4 Theoretical study of photodetachment spectra of anionic boron clusters. Nuclear dynamics

4.1 Introduction

The nuclear dynamics of boron clusters has not been studied in the literature except for B_3 [1] from our group. In this chapter we investigate how the complex structural properties of boron clusters detailed in Chapter 3 contribute to the nuclear dynamics underlying the observed photodetachment bands [2,3]. The crossings of various electronic states leading to CIs [7,8] often control the nuclear motion primarily on the participating electronic states and contribute to their overall band structures and time-dependent properties. The most critical consequence of CIs of electronic PESs is a break-down of the adiabatic BO theoretical formalism [9, 10]. In such circumstances it is therefore necessary to go beyond and examine nuclear motion concurrently with the electronic motion [7, 11–13]. The present study (wherever relevant) considers such a requirement. Moreover, the study here relies on a full quantum mechanical treatment including most of the relevant electronic and nuclear DOF.

The photodetachment spectrum of B_4^-, B_5^- and B_7^- considered here has been experimentally recorded by Wang and coworkers at three different (355, 266 and 193 nm) wavelengths of the probe laser photon [2, 3]. Depending on the energy of the probe photon at these wavelengths (3.496, 4.661 and 6.424 eV, respectively, in that order) the recorded vibronic bands reveal varied degree of energy resolution of the underlying peaks that could be attributed to the excitation of specific vibrational quanta. In the theoretical study detailed below, we tried to identify and assign the specific vibrational modes that contribute to a given spectral envelope predominantly.

The experimental photodetachment spectrum of B_4^- recorded by Wang and coworkers [2] reveals four broad bands in the 1.0-5.0 eV energy range. The recording at 355 nm photon wavelength revealed partially resolved structure of the $\widetilde{a}$ band whereas the $\widetilde{X}$ band revealed broad structure consistently at all three wavelengths of the photon used in the measurements. The latter is interpreted (through *ab initio* electronic structure calculations) to be due to a large geometry change of the neutral B_4 in its electronic ground state compared to that of B_4^- [2]. The detachment spectrum recorded at 266 nm revealed interesting and complex overlapping structures of the triplet $\widetilde{a}$ and $\widetilde{b}$ electronic states of B_4 [2]. While the origin of $\widetilde{X}$, $\widetilde{a}$ and $\widetilde{b}$ bands could be successfully predicted, the C band (as marked in the experiment [2]) that shows up in the 193 nm spectrum

could not be given a clear interpretation of its origin! In the present chapter, in addition to describing the detailed structure of the $\widetilde{X}$, $\widetilde{a}$ and $\widetilde{b}$ bands, we attempt to resolve this issue also.

The photodetachment spectrum of B_5^- recorded using same laser photons (as in case of B_4^-) revealed four bands in the 1.5-6.4 eV binding energy range [3]. While the three bands observed at lower energies are attributed to the $\widetilde{X}$, $\widetilde{A}$ and $\widetilde{B}$ doublet electronic states of B_5, the fourth one revealed much complex pattern observed at higher electron binding energies [3]. Resolved vibrational structures of the $\widetilde{X}$ and $\widetilde{A}$ bands are reported at 355 nm and 266 nm photon wavelengths, respectively. An adiabatic ionization energy of $\sim$ 2.33 eV is estimated from the resolved vibronic structure of the $\widetilde{X}$ state in which the 550 cm^{-1} vibrational mode is reported to make major progressions [3]. An average spacing of $\sim$ 530 cm^{-1} is estimated from the resolved vibronic structure of the $\widetilde{A}$ band observed in the 266 nm spectrum [3]. The $\widetilde{B}$ band, distinctly appeared in the 193 nm spectrum, is very broad and no vibrational progressions could be resolved. The complex features of the C band observed in the 193 nm spectrum is reported to originate from two one electron and several multielectron transitions. Inadequate energy resolution is one of the major shortcoming of the detachment spectrum of these small boron clusters. As pointed out by Wang and co-workers [2] that this is primarily due to low photodetachment cross sections of the light clusters and difficulty to produce them in cold conditions. The VDEs of B_5^- has been computed by the ROVGF as well as RCCSD(T) methods and excellent agreement with the experimental results has been reported [3]. The electron affinities of neutral B_4 and B_5 clusters and VDEs of their anions are calculated at CCSD(T) level and extrapolated upto CBS level [5, 6]. These reported results are in good accord with ours presented in Chapter 3.

The photodetachment spectrum of B_7^- recorded by Wang and co-workers reveals very complicated and congested band structure [4]. The spectrum recorded at 193 nm is reproduced in panel a of Fig. 4.20. A broad feature (X) at $\sim$2.85 eV and a very sharp and intense band (A) at $\sim$3.44 eV with a short vibrational progression with a spacing 480 (40) cm^{-1} are observed with the 355 nm laser photon. The adiabatic detachment energies $\sim$ 2.55 and 3.44 eV for X and A bands are observed in the experiment [4]. Four more bands B (3.71 eV), C (3.84 eV), D (4.05 eV) and E (4.21 eV) are observed at 266 laser energy. In 199 nm spectrum five more states appeared in a congested and narrow energy range of $\sim$ 0.7 eV. Overall total 11 distinct features are discernible in the 193 nm spectrum. The spectral intensities in the photodetachment spectrum of B_7^- found to be altered by the source of boron cluster beam [4], indicating the contribution of more than one low-lying isomers. Boldyrev *et al.* with his *ab initio* calculations confirmed that three isomers of B_7^- viz., a triplet hexagonal pyramidal (C_{6v}, $^3A_1$), a singlet pyramidal (C_{2v}, $^1A_1$) and a singlet planar (C_{2v}, $^1A_1$) contribute most to the recorded photodetachment band structure [4]. The above three isomers will be identified as I, II and III in the given order in the rest of this chapter.

In the present chapter we set out to investigate the detailed structure of each of the observed photodetachment bands of B_4^-, B_5^- and B_7^- by studying the underlying nuclear dynamics quantum mechanically using the techniques developed in 2 and employing the

Hamiltonians developed in Chapter 3. The excitations of vibrational modes, electronic nonadiabatic coupling effects and decay of the excited electronic states are examined and discussed in relation with the experimental observations mentioned above.

4.2 Results and Discussions

In this section we first report the complete broad band spectral envelopes of the electronic states of B_4, B_5 and B_7. These broad band envelopes are calculated by propagating WPs using the MCTDH program modules [14–17] and considering the complete Hamiltonians developed in Chapter 3. The *ab initio* electronic structure parameters reported therein are used (as are) without any adjustments. The theoretical results are compared with the reported experimental band structures [2, 3]. Subsequently, each of the broad spectral envelopes is critically examined at higher energy resolution. In this case the precise location of the vibronic levels is calculated by a time- independent matrix diagonalization approach employing the Lanczos algorithm [18] as stated above. The resolved band structures are also compared with resolved experimental results whenever available. Importantly, this exercise enabled us to identify the excitations of the vibrational modes underlying the broad experimental bands and assess the impact of electronic nonadiabatic effects on their overall structure. Finally, the decay of excited electronic states is examined and discussed.

4.2.1 Photodetachment bands of B_4^-

Broad band spectral envelope

The broad band spectrum of the low-lying electronic states of B_4 is shown in Fig. 4.1 along with the recorded 193 nm detachment spectrum of Wang and coworkers [2]. The theoretical results are obtained by using the six states diabatic Hamiltonian given in Eq. (3.7a) of Chapter 3 including all six vibrational degrees of freedom. Six separate WP propagations are carried out by preparing the WP initially in each of these electronic states and by numerically solving the time-dependent Schrödinger equation with the aid of the MCTDH program modules [14–17]. The technical details of the MCTDH WP propagations are given in Table 4.1. The time autocorrelation function data obtained from six calculations are combined in 1:1 statistical ratio, damped with an exponential function, $e^{-\frac{t}{\tau}}$ (with a damping time τ= 11 fs) and finally Fourier transformed to generate the spectral envelopes shown in the panel a and b of Fig. 4.1. While the set of Hamiltonian parameters (cf. Tables 3.17 to 3.20 of Chapter 3) obtained with the UB3LYP optimized equilibrium geometry of B_4^- used to calculate the spectrum in panel a, the same (cf. Tables 3.21 to 3.24 of Chapter 3) obtained with the ROMP2 optimized equilibrium geometry are used to calculate the spectrum in panel b. It can be seen that both the results agree extremely well with each other. This additionally demonstrates negligible spin contamination in the theoretical results presented here. Although the theoretical results in Figs. 4.1(a-b) obtained by using reference geometry optimized by two different methods agree extremely well with each other, the VDEs obtained from the

Table 4.1: The normal mode combinations, sizes of the primitive and single particle bases used in the WP propagation (using the MCTDH program modules [14–17]) on the $\widetilde{X}$-$\widetilde{a}$-$\widetilde{b}$-$\widetilde{A}$-$\widetilde{c}$-$\widetilde{B}$ electronic manifold of B_4^- using the Hamiltonian of Eq. (3.7a) of Chapter 3.

S.No	Normal modes	Primitive basis	SPF basis
1	ν_1,ν_3	(10,8)	[6,4,4,6,10,15]
2	ν_2,ν_5	(12,4)	[10,10,4,10,4,4]
3	ν_4,ν_6	(4,8)	[6,8,8,6,4,4]

ROMP2 optimized reference geometry seem to reproduce the experiment slightly better (cf., Table 3.3 of Chapter 3) , Therefore, we have adjusted the VDE values obtained with the UB3LYP optimized geometry to those of the ROMP2 reference values in calculating the band structure presented in panel a.

It can be seen that the experimental features of the recorded detachment spectrum (reproduced from ref. [2] in panel c) are reproduced very well by both sets of theoretical results presented in Fig. 4.1. We reiterate that the $\widetilde{X}$ band has been found to be broad and diffuse in all three different wavelengths of the probe laser photon used in the experiment [2]. The broad structure of the $\widetilde{X}$ band is attributed to a large geometry change of the equilibrium minimum configuration of the electronic ground state of B_4^- and B_4 [2].

The second broad band has been attributed to the vibronic structure of the $\widetilde{a}^3B_{2u}$ and $\widetilde{b}^3B_{1u}$ electronic states of B_4 based on their VDEs. It can be seen from Table 3.18 of Chapter 3 that these two states are coupled through the ν_6 vibrational mode of b_{3g} symmetry. Also, the bilinear interstate coupling parameter along $\nu_3\nu_4$ vibrational modes is nonzero for these states. It is discussed in Chapter 3 that the energetic minimum of the $\widetilde{a}$-$\widetilde{b}$ CIs occurs at $\sim$ 3.34 eV, which is quasi-degenerate with the minimum of the $\widetilde{b}$ state. This results into the highly overlapping and diffuse structure of the second detachment band of B_4^-. It can be seen that the observed asymmetry of this band is very well reproduced by the present theoretical results.

The third detachment band of B_4^- has been found to be formed by the $\widetilde{A}$, $\widetilde{c}$ and $\widetilde{B}$ electronic states of B_4. All these three states are located vertically within $\sim$1.0 eV of energy (cf., Table 3.3 of Chapter 3). The coupling of the singlet $\widetilde{A}$ and $\widetilde{B}$ states is not found from the electronic structure data. The triplet $\widetilde{c}$ state is however, strongly coupled to the $\widetilde{b}$ state through the ν_5 vibrational mode (cf., Table 3.18 of Chapter 3). Despite this, the energetic minimum of the $\widetilde{b}$-$\widetilde{c}$ CIs occurs at $\sim$ 11.33 eV which is $\sim$ 7.24 eV above the $\widetilde{c}$ state minimum. It is therefore very unlikely to expect any impact of the $\widetilde{b}$-$\widetilde{c}$ CIs on the overall structure of the third detachment band. Although the theoretical structure of this band in Fig. 4.1 reveals an overall agreement with the experiment, there remains several discrepancies:
(i) the structures above $\sim$ 3.7 eV and below $\sim$ 4.25 eV seen in the theoretical spectrum are missing in the experimental band,
(ii) the theoretical band reveals distinct peak structure, whereas the experimental band

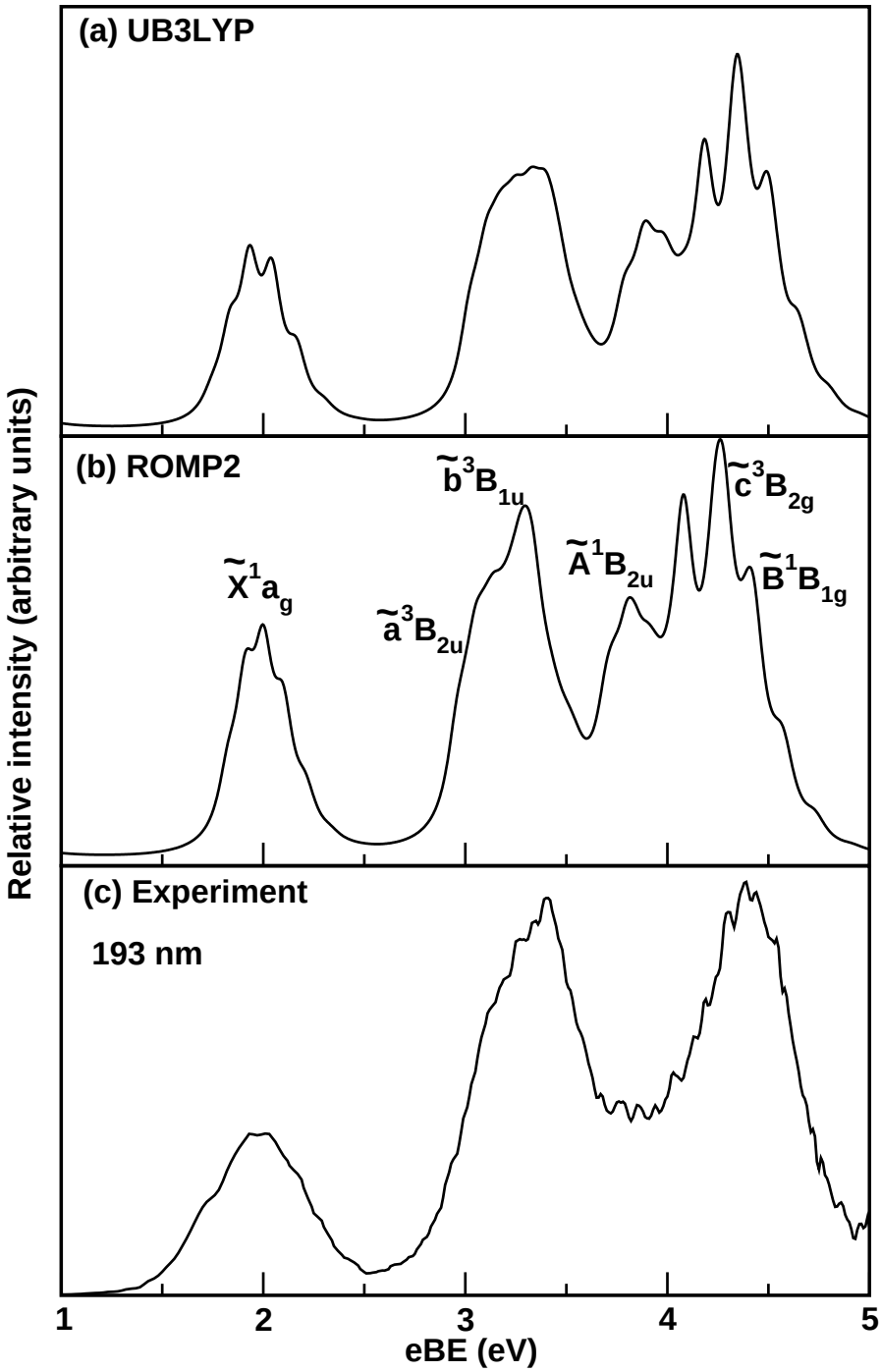

Figure 4.1: The photodetachment bands of B_4^- obtained by the time-dependent WP propagation approach (see text for details) and employing the complete vibronic Hamiltonian of Eq. 3.7a of Chapter 3. The theoretical results obtained by using the UB3LYP and ROMP2 reference geometries are shown in panel a and b, respectively. The symmetry of the final electronic states (of neutral B_4) at the reference equilibrium configuration is indicated in panel a. The 193 nm experimental recording of Wang and coworkers is reproduced from Ref. [2] and shown in panel b.

Table 4.2: The number of harmonic oscillator basis function used in the calculation of the stick vibronic spectrum of the mentioned electronic states of B_4.

S.NO	State(s)	No. of HO basis along ν_1,ν_2,ν_3,ν_4,ν_5,ν_6
1	$\widetilde{X}^1A_g$	9,100,2,2,2,2
2	$\widetilde{a}^3B_{2u}$	10,200,2,2,2,2
3	$\widetilde{b}^3B_{1u}$	80,4,2,2,2,2
4	$\widetilde{A}^1B_{2u}$	5,125,2,2,2,2
5	$\widetilde{c}^3B_{2g}$	320,6,2,2,2,2
6	$\widetilde{B}^1B_{2g}$	250,6,2,2,2,02
7	$\widetilde{X}^1A_g$-$\widetilde{A}^1B_{2u}$	30,300,10,10,2,2
8	$\widetilde{a}^3B_{2u}$-$\widetilde{b}^3B_{1u}$	10,150,6,6,45,2

is almost structureless.

Small detachment cross sections obtained in the experimental measurements [2] and the neglect of probable contribution from dynamic spin- orbit interactions of the triplet $\widetilde{c}$ state with the participating singlet states may be the reasons for the observed discrepancy. The latter issue is presently being examined in our group.

Interpretation of the structure of the detachment bands

The photodetachment bands of B_4^- presented in Fig. 4.1(a) are examined here in detail to reveal the contributions of the vibrational modes to the broad envelopes. A time-independent matrix diagonalization method (as discussed in Sec. 2.4.1) of Chapter 2 is employed for this purpose. This method yields the precise location of the vibronic lines within the accuracy of the present theoretical model. The technical details of the calculation of all the stick vibronic spectra presented in this section are given in Table 4.2. The calculated stick spectrum of a given state is convoluted with a Lorentzian function with 15 meV FWHM to generate the corresponding envelope. All theoretical calculations are carried out with the Hamiltonian parameters presented in Chapter 3 (cf., Tables 3.17 to 3.20 of Chapter 3) without any adjustments.

The vibrational structure of the $\widetilde{X}^1A_g$ electronic state of B_4 without including its coupling with the neighboring states is shown in panel a of Fig. 4.2. Both the symmetric vibrational modes ν_1 and ν_2 form progressions in this band. The dominant progression is formed by the ν_2 vibrational mode. The peaks are 1590 and 423 cm^{-1} spaced corresponding to the frequency of combination (ν_1+ν_2) and ν_2 vibrational modes, respectively. As stated above that a very broad structure of this band is observed in the experiment. The best, resolved band structure obtained in the 355 nm recording is given in panel b of Fig. 4.2. It can be seen that the overall width of the experimental band is in good accord with the theoretical results. The theoretical VDEs of $\sim$ 1.903 eV (cf., Table 3.3 of Chapter 3) is also in good agreement with the experimental estimate of $\sim$ 1.99 $\pm$ 0.05 eV [2]. This estimate is slightly in better agreement with the results obtained

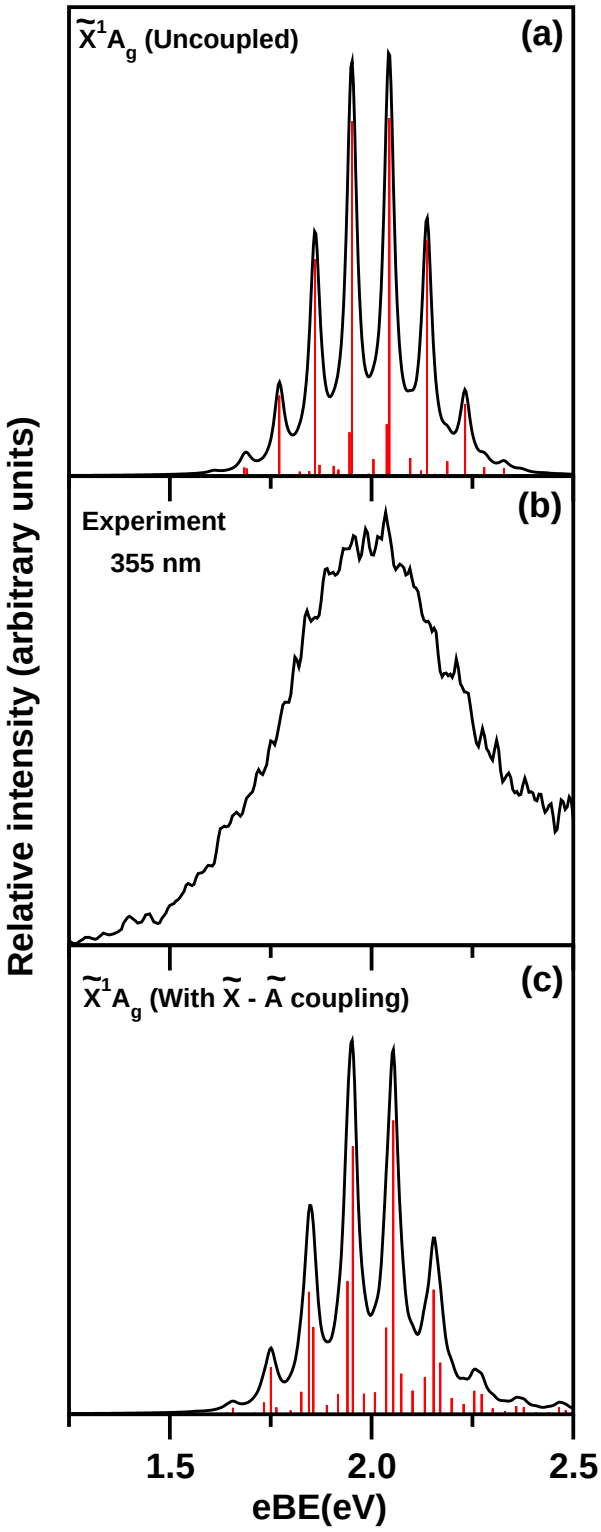

Figure 4.2: The stick vibronic spectrum of the $\widetilde{X}^1A_g$ electronic state of B_4 along with the convoluted spectral envelope. The spectrum obtained by excluding all couplings with the neighboring states is given in panel a. The best resolved 355 nm experimental recording is reproduced from Ref. [2] and shown in panel b. The spectrum obtained by including the coupling with the $\widetilde{A}$ electronic state is shown in panel c.

Table 4.3: Optimized equilibrium geometry parameters of the electronic ground state of B_4. The results available in the literature [2] are also included in the table for comparison.

S.No	Equilibrium parameters for B_4 in the $\widetilde{X}^1A_g$ state	Ref. [2]	Ref. [5][a]	This work B3LYP/aug-cc-pVTZ
1	E_{total}/hatree	-99.156	-98.919	-99.137
2	R(B1-B2)/angstrom	1.523	1.5754	1.519
3	R(B1-B3)/angstrom	-	1.9334	1.889
4	R(B2-B4)/angstrom	-	-	2.399
5	$\angle B1-B2-B3$ /degrees	76.50	75.7	76.5
6	$\angle B2-B1-B4$ /degrees	-	104.3	103.5

[a] The total electronic energy calculated at CCSD(T) and extrapolated to complete basis set upto doubles, triples and quadrapole zeta (CBS(DTQ)) approximation. The geometry parameters reported at CCSD(T)/aug-cc-pVTZ level of theory.

from ROMP2 and UCCSD(T) optimized reference geometry. It is discussed in Chapter 3 that the $\widetilde{X}^1A_g$ state is not coupled (in first-order) with the other two singlet states $\widetilde{A}$ and $\widetilde{B}$. A non-zero bilinear interstate $\widetilde{X}$-$\widetilde{A}$ coupling along $\nu_3\nu_6$ combination modes has been found (cf., Tables 3.19 and 3.23 of Chapter 3). However, no noticeable impact of this coupling on the structure of the $\widetilde{X}$ band is observed. The $\widetilde{X}$ band obtained by including the $\widetilde{X}$-$\widetilde{A}$ coupling is shown in panel c. The significant geometry change (along the B-B-B angle) from the anion to the neutral ground electronic state is obvious from the structure of $\widetilde{X}$ band. The intensity of the origin (0-0) peak is very small and the maximum shifts to the $4^{th}/5^{th}$ quantum of excitation of the ν_2 vibrational mode. We also optimized the equilibrium geometry of B_4 in the $\widetilde{X}$ state, at the B3LYP/aug-cc-pVTZ level of theory. The optimized geometry parameters are given in Table 4.3 and compared with the available literature data [3,5]. It can be seen in comparison with the optimized geometry parameters of the anionic $\widetilde{X}^2B_{1u}$ state (cf., Table 3.1 of Chapter 3) that all the adjacent B-B bonds are shortened by 0.04 angstrom[1] and the B-B-B angles are reduced by $\sim 13^\circ$ in the neutral ground state. The bond between the diagonally opposite B atoms elongates by ~ 0.24 angstroms in the neutral ground state.

The vibrational structures of the uncoupled $\widetilde{a}^3B_{2u}$ and $\widetilde{b}^3B_{1u}$ electronic states of B_4 are shown in panel a and b of Fig. 4.3, respectively. It can be seen from Table 3.18 of Chapter 3 that the coupling strength of both the symmetric vibrational modes is very small in the $\widetilde{b}$ state whereas, the vibrational mode ν_2 has a large coupling strength in the $\widetilde{a}$ state. The bilinear $\nu_1\nu_2$ coupling parameter in the $\widetilde{a}$ state is $\sim$10 times larger than that in the $\widetilde{b}$ state (Table 3.19 of Chapter 3). As a result distinct progression of the ν_2 vibrational mode can be observed in the spectrum of the $\widetilde{a}$ state (panel a). The peaks are $\sim 741\ cm^{-1}$ spaced, corresponding to the frequency of the ν_2 vibrational mode in the $\widetilde{a}$ state. In contrast, the spectrum of the $\widetilde{b}$ state (panel b) shows only weak

[1]Due to some conflict in latex packages, I am unable to write the symbol of angstrom.

structures. Very weak excitation of ν_1 vibrational modes at an energy spacing (from 0-0 peak) of $\sim$ 1150 cm^{-1} can be seen from the spectrum of panel b of Fig. 4.3. The band structure of the $\widetilde{a}$ and $\widetilde{b}$ electronic states, is found to be very broad and overlapping in the experimental recording [2]. As already discussed that the $\widetilde{a}$ and $\widetilde{b}$ states are coupled through the ν_6 (Table 3.18 of Chapter 3) and $\nu_3\nu_4$ (Table 3.19 of Chapter 3) vibrational modes, and the energetic minimum of $\widetilde{a}$-$\widetilde{b}$ CIs is quasi-degenerate with the minimum of the $\widetilde{b}$ state. Strong nonadiabatic mixing of the $\widetilde{a}$ and $\widetilde{b}$ electronic states therefore causes a blurring of the distinct weak vibrational structure of the uncoupled $\widetilde{b}$ state. The coupling strength of the $\widetilde{b}$ with the $\widetilde{c}$ state is also very large (Table 3.18 of Chapter 3), however, these two states are vertically $\sim$ 1.0 eV apart (cf. Table 3.3 of Chapter 3). Also the minimum of the $\widetilde{b}$-$\widetilde{c}$ CIs occurs at much high energy, $\sim$ 7.24 eV above the minimum of the $\widetilde{b}$ state and does not have any impact on the spectrum. The $\widetilde{a}$-$\widetilde{b}$ coupled states spectrum is plotted in panel c of Fig. 4.3. Some increase of the spectral line density can be immediately seen from the spectrum of panel c. The excitation of non totally symmetric mode ν_6 with an energy spacing of $\sim$ 1004 cm^{-1} is estimated from the irregular spectral progression.

It is shown in Fig. 4.1 and discussed therein that the third detachment band of B_4^- is formed by three energetically close-lying ($\widetilde{A}^1B_{2u}$, $\widetilde{c}^3B_{2g}$ and $\widetilde{B}^1B_{2g}$) electronic states of B_4. These states are found to be decoupled from each other (except the possible dynamic spin-orbit coupling which is not explored in this chapter) or coupling of any of these states (if exists) with a lower one occurs at very high energies (for example, the $\widetilde{b}$-$\widetilde{c}$ coupling, see Chapter 3 for details) and does not play any role in the energy range of the detachment bands studied here. The composite third detachment band of B_4 obtained by combining the stick spectrum of the $\widetilde{A}$, $\widetilde{c}$ and $\widetilde{B}$ electronic states is shown in the panel a of Fig. 4.4. The 193 nm and 266 nm experimental bands of Ref [2] are shown in panel b of Fig. 4.4. It can be seen in comparison that in the 193 nm spectrum the detachment cross section of the $\widetilde{A}$ state is very small. Whereas, distinct vibrational structure of the $\widetilde{A}$ band is obtained in the theoretical results. The 266 nm experimental spectrum, however reveals some structure in this region. At high energies the broad band experimental envelope agrees fairly well with the overall composite spectrum of the $\widetilde{c}$ and $\widetilde{B}$ electronic states of B_4. The vibrational mode ν_2 in the $\widetilde{A}$ and ν_1 in the $\widetilde{c}$ and $\widetilde{B}$ electronic states from dominant progressions. Peak spacings of $\sim$ 767, $\sim$ 1234 and $\sim$ 1237 cm^{-1} are found corresponding to the frequency of these modes in the mentioned electronic states, respectively.

Internal conversion dynamics

Dynamics of the electronic excited states of B_4 cluster is examined in terms of time-dependence of adiabatic electronic populations recorded in the WP calculations. The time dependence of the adiabatic populations when the WP prepared on $\widetilde{X}$, $\widetilde{a}$, $\widetilde{b}$, $\widetilde{A}$, $\widetilde{c}$ and $\widetilde{B}$ electronic states is shown in panel a-f of Fig. 4.5. Except for the $\widetilde{a}^3B_{2u}$ and $\widetilde{b}^3B_{1u}$ electronic states the nonadiabatic coupling effects are found not very insignificant in B_4. The coupling between the $\widetilde{A}^1B_{2u}$ and $\widetilde{X}^1A_g$ states through the intermode bilinear ($\nu_3\nu_6$)

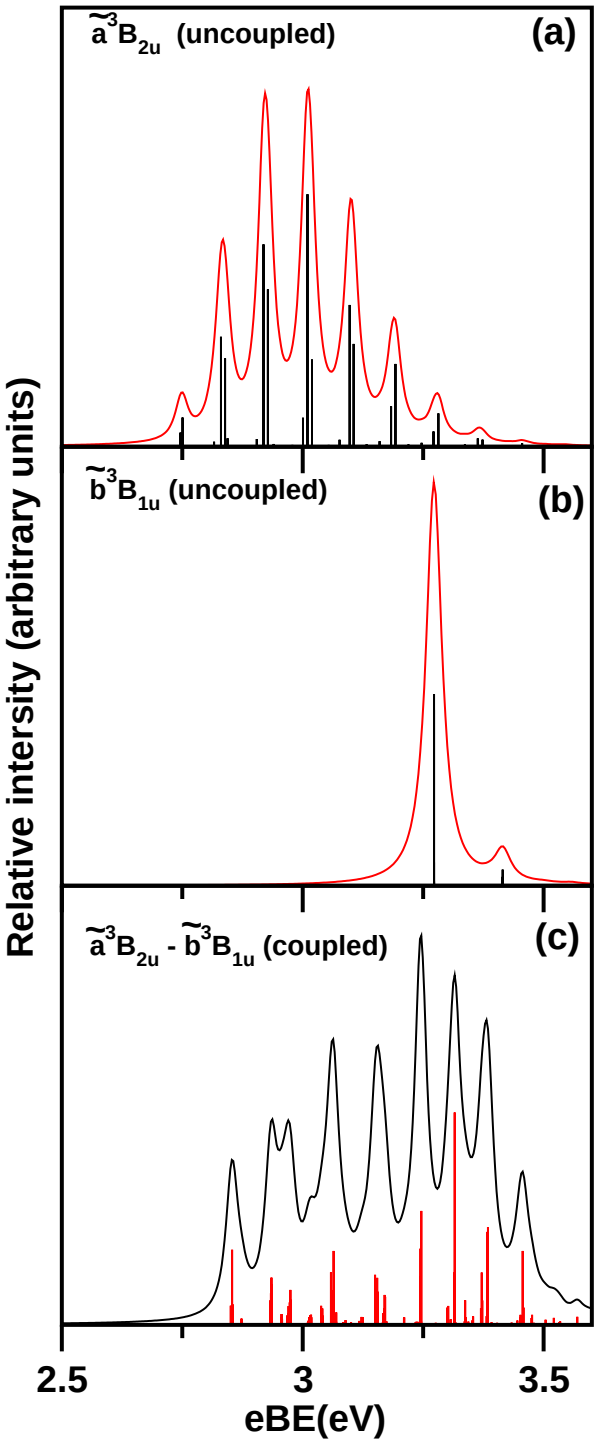

Figure 4.3: Stick vibronic spectrum and the corresponding convoluted envelope. The spectra of uncoupled $\widetilde{a}$ and $\widetilde{b}$ states are shown in panels a and b, respectively. The entire $\widetilde{a}$-$\widetilde{b}$ spectrum obtained by including nonadiabatic coupling between them is shown in panel c.

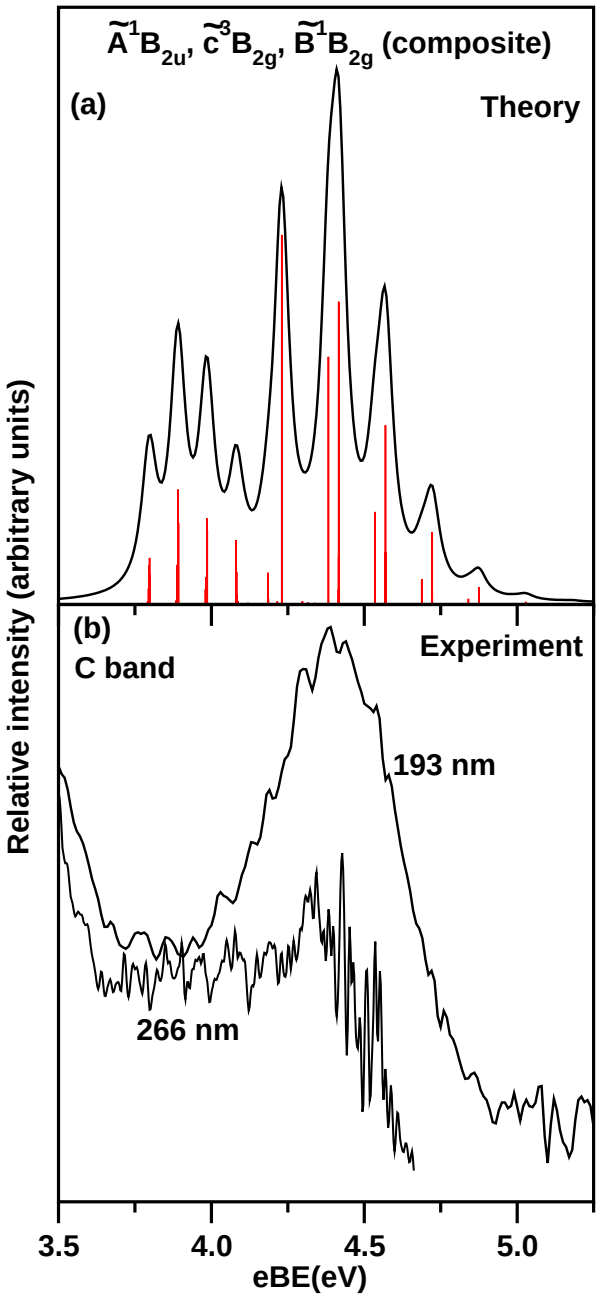

Figure 4.4: Composite stick vibronic spectrum and the convoluted envelope (panel a) of the $\widetilde{A}$, $\widetilde{c}$ and $\widetilde{B}$ electronic states of B_4. The 193 and 266 nm experimental recordings of Ref. [2] are shown in panel b for comparison.

coupling term (cf., Table 3.19 of Chapter 3) has been found to have very mild effects on the vibronic energy level structure of these electronic states only. Less than 1 % of the electronic population flows to the $\widetilde{X}$ state when the WP is initially prepared on the $\widetilde{A}$ state in this case.

In contrast to the above scenario, the nonadiabatic coupling appears to have significant effect on the dynamics of the $\widetilde{a}^3B_{2u}$ and $\widetilde{b}^3B_{1u}$ electronic states. To assess these coupling effects on the nonradiative internal conversion dynamics we show the time-dependence of the adiabatic and diabatic electronic populations in Fig. 4.6. The adiabatic (thick solid line) and diabatic (thin dashed line) electronic populations for an initial location of the WP on the $\widetilde{a}$ and $\widetilde{b}$ diabatic states are shown in panel a and b of Fig. 4.6, respectively. It can be seen from panel a of Fig. 4.6(a) that the diabatic population of the $\widetilde{a}$ state starts from 1.0 and that of the $\widetilde{b}$ state from 0.0 at t=0. The population of the $\widetilde{a}$ state flows to the $\widetilde{b}$ state in time and fluctuates around 0.8 at longer times. The recurrences in the diabatic population curves indicate WP moves back and forth between the two states in a time scale of $\sim$ 49 fs which nearly corresponds to the period of the ν_2 vibrational mode. It can be seen from the Table 3.18 of Chapter 3 that the latter mode is strongly active in the $\widetilde{a}$ state of B_4. Since a diabatic state is an admixture of the two (lower and upper) adiabatic states, the initial location of the WP on the diabatic state corresponds to 70 % and 30 % population of the two adiabatic states. The upper and lower adiabatic population curves in panel b correlates to the $\widetilde{a}$ and $\widetilde{b}$ states of B_4, respectively. The oscillations in the adiabatic population curves are much smaller in magnitude compared to those in the diabatic population curves, and relatively less significant population flows to the adiabatic states in this situation.

The adiabatic and diabatic electronic populations for an initial location of the WP on the $\widetilde{b}^3B_{1u}$ electronic state (diabatic) are plotted in panel b of Fig. 4.6. The lower thin dashed and thick solid curves represent diabatic and adiabatic population, respectively, of the $\widetilde{b}$ state whereas the same for the $\widetilde{a}$ state are represented by the same two curves in the upper part of panel b. In contrast to the population curves of panel a, a large fraction of population flows to both the electronic states in this case. This is because the equilibrium minimum of the $\widetilde{b}$ state is near degenerate to the minimum of the $\widetilde{a}$-$\widetilde{b}$ CIs (cf., Chapter 3). The diabatic population of the $\widetilde{b}$ state starts from 1.0 at t=0. The corresponding adiabatic population is $\sim$ 0.7 at t=0. A sharp decay of population occurs within $\sim$ 10 fs followed by the quasi-periodic recurrences. The diabatic population of the $\widetilde{a}$ state on the other hand starts from zero at t=0 and exhibits quasi-periodic recurrences at longer times. The corresponding adiabatic population also exhibits oscillatory pattern starting at $\sim$ 0.3 at t=0. The initial sharp decrease of population relates to a decay rate of the $\widetilde{b}$ state of $\sim$ 14 fs ($\sim$ 7 fs) in the diabatic (adiabatic) picture.

We note that the coupling parameters of the Hamiltonian derived from the ROMP2 optimized reference geometry (cf., Tables 3.21 to 3.24 of Chapter 3) are almost identical to those obtained from the UB3LYP optimized reference geometry (cf., Tables 3.17 to 3.20 of Chapter 3). The stationary points of the $\widetilde{a}$-$\widetilde{b}$ are also nearly identical in the two sets of results (cf., Chapter 3). The electronic population dynamics discussed above also remains same when calculated with the parameters of (cf., Tables 3.17 to 3.20).

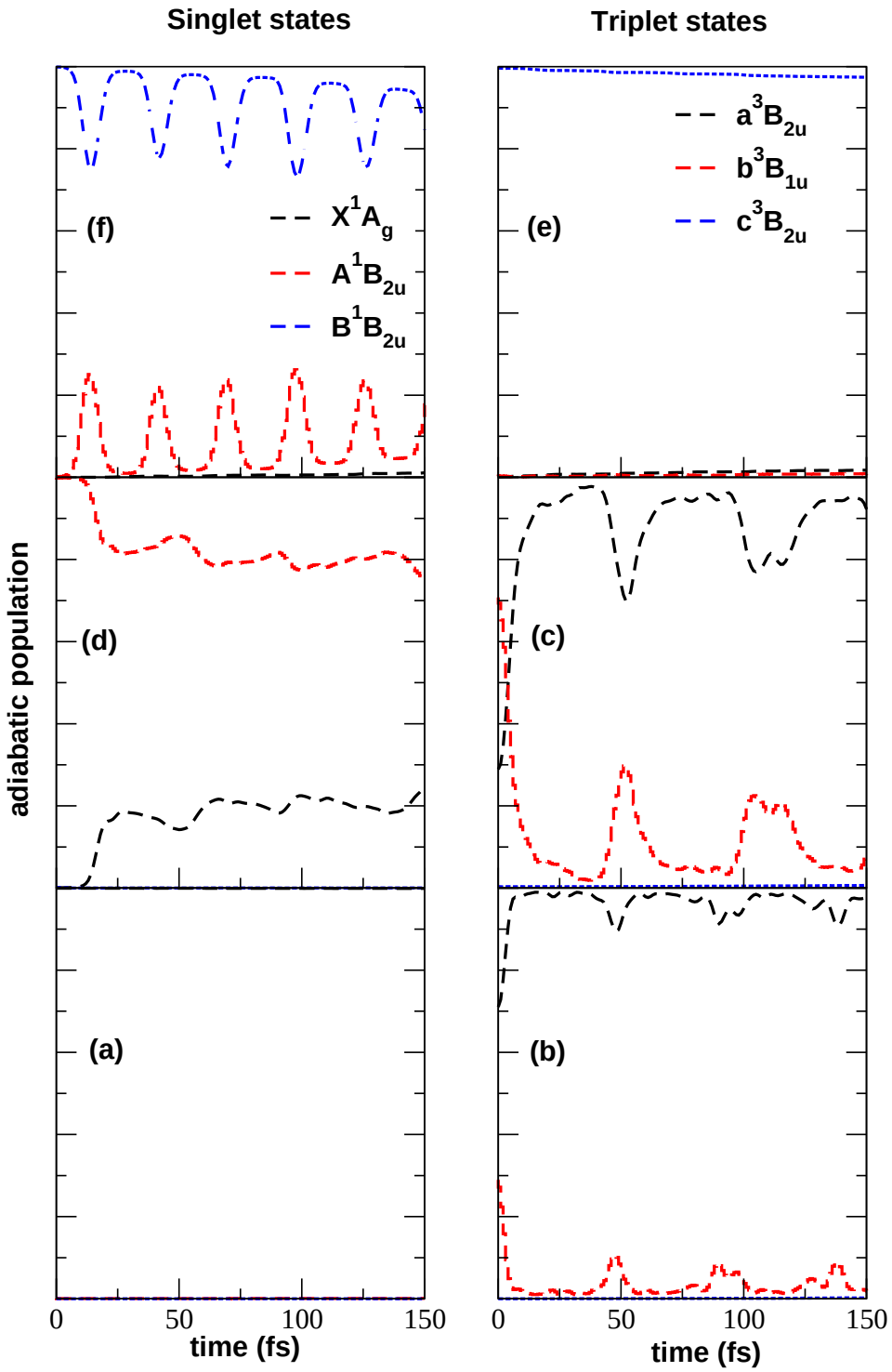

Figure 4.5: Time-dependence of the adiabatic electronic populations in the coupled surface dynamics of B_4. The electronic populations for an initial preparation of the WP on the $\widetilde{X}$, $\widetilde{a}$, $\widetilde{b}$, $\widetilde{A}$, $\widetilde{c}$ and $\widetilde{B}$ electronic states are shown in panel a-e, respectively (see text for details).

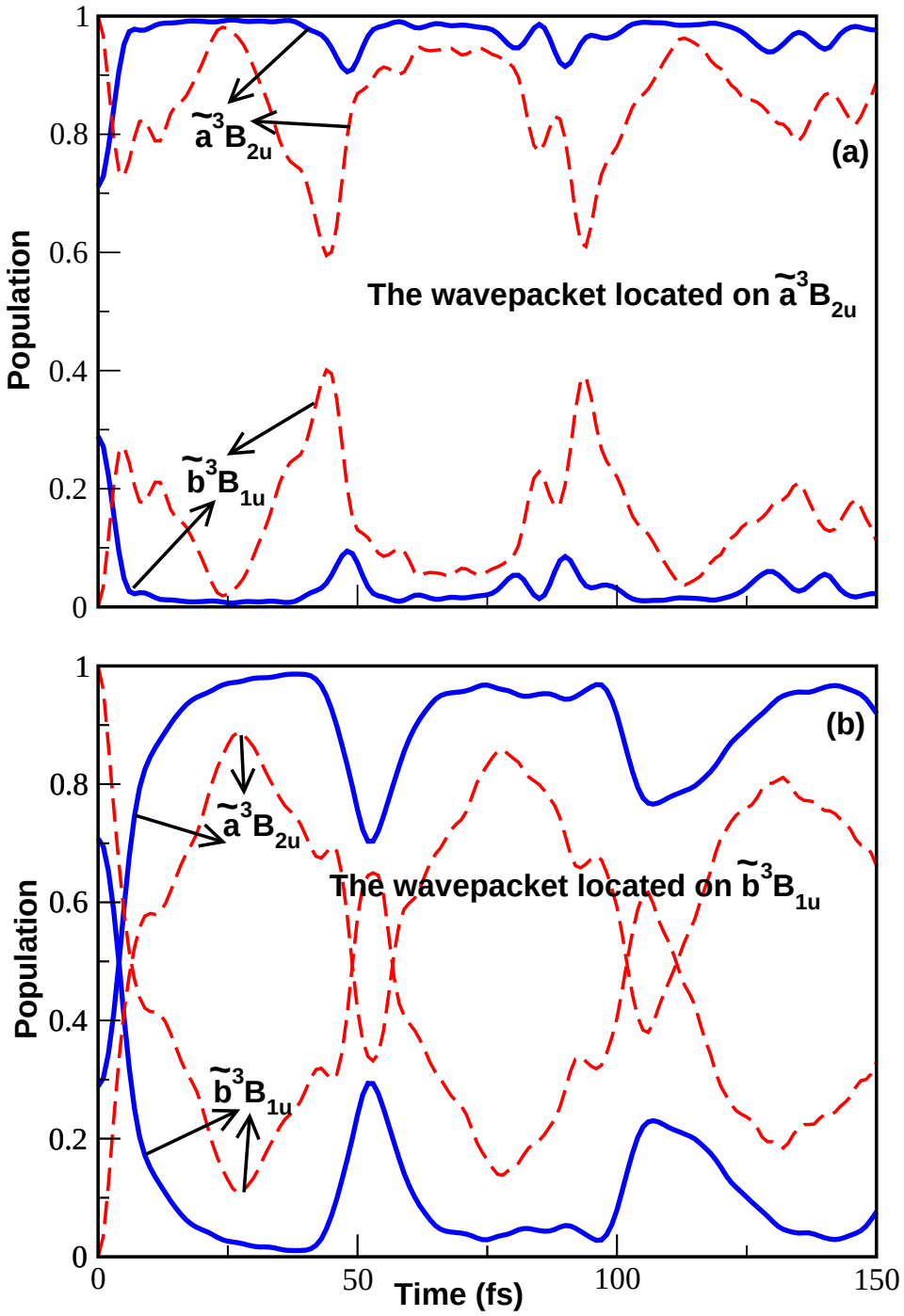

Figure 4.6: Time-dependence of the diabatic (dashed lines) and adiabatic (solid lines) electronic populations in the coupled surface dynamics of B_4. The electronic populations for an initial preparation of the WP on the $\widetilde{a}$ and $\widetilde{b}$ electronic states are shown in panel a and b, respectively (see text for details).

Table 4.4: The normal mode combinations, sizes of the primitive and single particle bases used in the WP propagation (using the MCTDH program modules [14–17]) on the $\widetilde{X}$-$\widetilde{A}$-$\widetilde{B}$-$\widetilde{C}$-$\widetilde{D}$-$\widetilde{E}$ electronic states of B_5 using Hamiltonian of Eq. (3.9) of 3.

S.No	Normal modes	Primitive basis	SPF basis
1	ν_1,ν_3,ν_7	(6,10,8)	[8,8,10,10,4,10]
2	ν_2,ν_6,ν_8	(10,6,6)	[10,8,10,8,4,8]
3	ν_4,ν_5,ν_9	(8,4,8)	[4,10,8,8,10,10]

4.2.2 Photodetachment bands of B_5^-

Broad band spectral envelope

The broad band spectral envelope of B_5 obtained by WP propagations using the MCTDH method [14–17] is shown in the panel a of Fig. 4.7. The 193 nm experimental recording of Ref. [2] is shown in the panel b of Fig. 4.7. Six separate WP calculations are carried out with six different choices of initial state, the time autocorrelation functions derived from these calculations are then combined, damped with an exponential function ($e^{-\frac{t}{\tau}}$, with τ_r=11 fs) and Fourier transformed to generate the spectral envelopes shown in panel a. The full Hamiltonian and its parameters given in Eq. 3.9 and Tables 3.25 to 3.27 respectively of Chapter 3, are used in the WP calculations. The technical details of the WP calculations using MCTDH program modules [14–17] are given in Table 4.4. It can be seen from Fig. 4.7 that the broad band theoretical spectrum agrees fairly well with the experimental band structures.

While the 193 nm experimental spectrum [3] reveals broad structures of all detachment bands (with a partial resolution of the C band), resolved vibronic structures of the $\widetilde{X}$ and $\widetilde{A}$ states are reported in the 355 nm and 266 nm recordings, respectively. The individual band structures at higher energy resolutions are discussed later in the text. The first band is found to originate from photodetachment of B_5^- to the $\widetilde{X}^2B_2$ electronic state of B_5. An adiabatic detachment energy of $\sim$ 2.33 eV is reported for this band [3]. The second and third bands are found to represent the vibronic structures of the $\widetilde{A}^2A_1$ and $\widetilde{B}^2B_2$ electronic states of B_5. The third band marked C in the energy range between 4.7-6.2 eV seems to reveal features originating from both one electron detachment channels as well as multi-electron transitions [3]. No assignment of these features are available from an analysis of the experimental spectrum [3]. We have found two one-electron detachment channels leading to $\widetilde{C}^2A_1$ and $\widetilde{D}^2B_1$ electronic states of B_5 and several shake-up states (electron detachment followed by electron reorganization) exist in this energy range. A careful examination of the details of these shake-up states is out of the scope of the present chapter and is left to a future work. We however mention that along with one electron detachment states $\widetilde{C}$ and $\widetilde{D}$ we considered the shake-up state $\widetilde{E}$ in the theoretical calculations of the C band. The latter state is found to have some contribution in the observed structure of the C band between $\sim$ 5.4-6.0 eV. The structures between $\sim$ 4.7-5.4 eV are found to be formed by the $\widetilde{C}$ and $\widetilde{D}$ electronic states

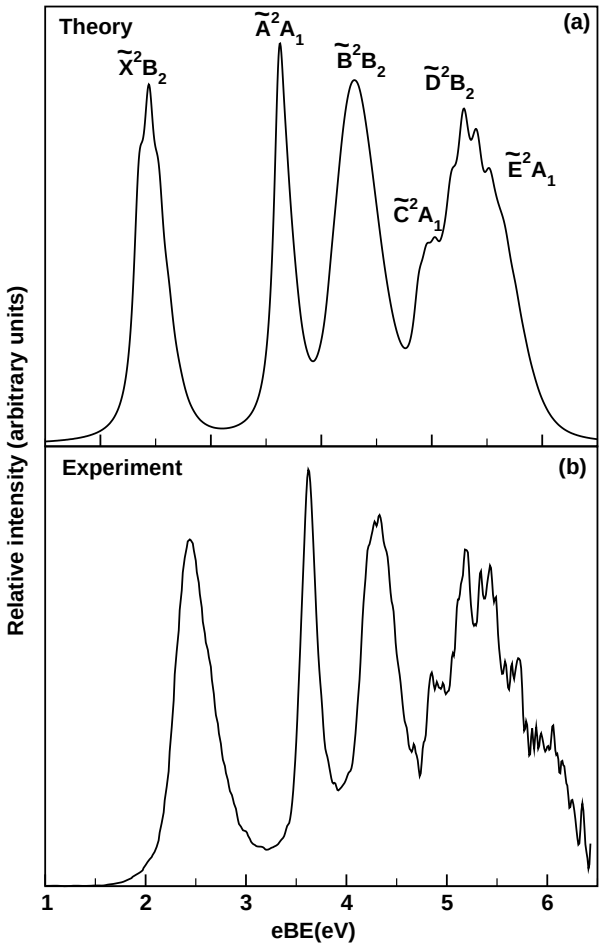

Figure 4.7: Broad band spectral envelope (panel a) of the low-lying six electronic states of B_5 cluster obtained by the WP propagations using the complete Hamiltonian of Eq. 3.9 of Chapter 3 (see text for details). The symmetry designation of the electronic states at the reference C_{2v} configuration is given in the panel. The 193 nm experimental recording of Ref. [3] is shown in panel b. The relative heights of the theoretical envelopes are adjusted to the maximum relative to the electron detachment probabilities extracted from the experimental spectrum.

of B_5.

As discussed in Chapter 3 that the existence of the $\widetilde{C}^2A_1$ state does not have any clear evidence in the literature. In our CASSCF(11,10)-MRCI calculations we found this state at $\sim$ 4.96 eV of VDE. Now, the hump in the experimental results, between $\sim$ 4.5-5.0 eV can only be obtained with the CASSCF(11, 10)-MRCI results, as shown in Fig. 4.7. We therefore strongly believe (as confirmed by more test calculations) the existence of the $\widetilde{C}^2A_1$ state in this energy region. The OVGF calculations clearly overestimate the energy of this state and lead to a conflicting energetic ordering.

Table 4.5: The number of harmonic oscillator basis function used in the calculation of the stick vibronic spectrum of the mentioned electronic states of B_5.

S.NO	State	No of HO basis along ν_1,ν_2,ν_3,ν_4,ν_6,ν_7,ν_8,ν_9
1	$\widetilde{X}^2B_2$	5,5,76,19,2,3,3,3
2	$\widetilde{A}^2A_1$	3,8,3,16,2,3,3,3
3	$\widetilde{B}^2B_2$	15,7,26,12,2,3,3,3
4	$\widetilde{C}^2A_1$	50,4,7,60,2,3,3,3
5	$\widetilde{D}^2B_1$	3,100,6,10,2,3,3,3
6	$\widetilde{E}^2A_1$	15,3,22,11,2,3,3,3
7	$\widetilde{X}^2B_2$-$\widetilde{A}^2A_1$	4,3,25,12,2,10,3,15
8	$\widetilde{X}^2B_2$-$\widetilde{C}^2A_1$	4,3,12,6,2,4,9,54
9	$\widetilde{X}^2B_2$-$\widetilde{E}^2A_1$	18,3,26,12,2,3,3,34
10	$\widetilde{A}^2A_1$-$\widetilde{B}^2B_2$	12,8,32,18,2,3,10,3
11	$\widetilde{B}^2B_2$-$\widetilde{C}^2A_1$	8,6,20,12,2,3,3,40
12	$\widetilde{B}^2B_2$-$\widetilde{E}^2A_1$	6,4,16,9,2,2,2,36
13	$\widetilde{D}^2B_1$-$\widetilde{E}^2A_1$	10,20,30,15,40,2,2,2

Interpretation of the structure of the detachment bands

The vibrational fine structures underlying the broad detachment bands of B_5^- shown in Fig. 4.7 are examined here. The time-independent matrix diagonalization approach is employed to calculate the stick line spectrum underlying the broad spectral envelopes. In Table 4.5, the technical details of the calculation of each spectrum shown below are given. Each spectrum is converged with respect to the parameters given in this table. The stick spectra presented below are convoluted with a Lorentzian function of 15 meV FWHM to generate the respective spectral envelopes.

The vibrational structure of the $\widetilde{X}$ state of B_5 in absence of coupling with its neighboring states is shown in panel a and the resolved 355 nm experimental recording of Ref [3] is shown in panel b of Fig. 4.8. It can be seen in comparison that the theoretical results are in very good agreement with the experimental band structure of the $\widetilde{X}$ state. The weak feature observed at $\sim$ 2.24 eV in the experiment and attributed to a hot band understandably cannot be seen in the theoretical results. From the data given in Table 3.25 of Chapter 3, the excitation of vibrational modes ν_3 and ν_4 can be expected in this band. The excitation of the ν_3 mode is stronger than that of ν_4. Line spacings of $\sim$ 724 and $\sim$ 658 cm^{-1} corresponding to the frequency of these modes, respectively, can be extracted from the theoretical spectrum. A vibrational progression of $\sim$ 550 cm^{-1} has been estimated from the experimental band structure [3] of the $\widetilde{X}$ state.

It can be seen from the data given in Table 3.26 that $\widetilde{X}$ state is coupled (in first-order) with the $\widetilde{A}^2A_1$ state via ν_7 and ν_9 vibrational modes, with the $\widetilde{C}^2A_1$ state via the ν_7, ν_8 and ν_9 vibrational modes and with $\widetilde{E}^2A_1$ state via the ν_7 vibrational mode of b_2

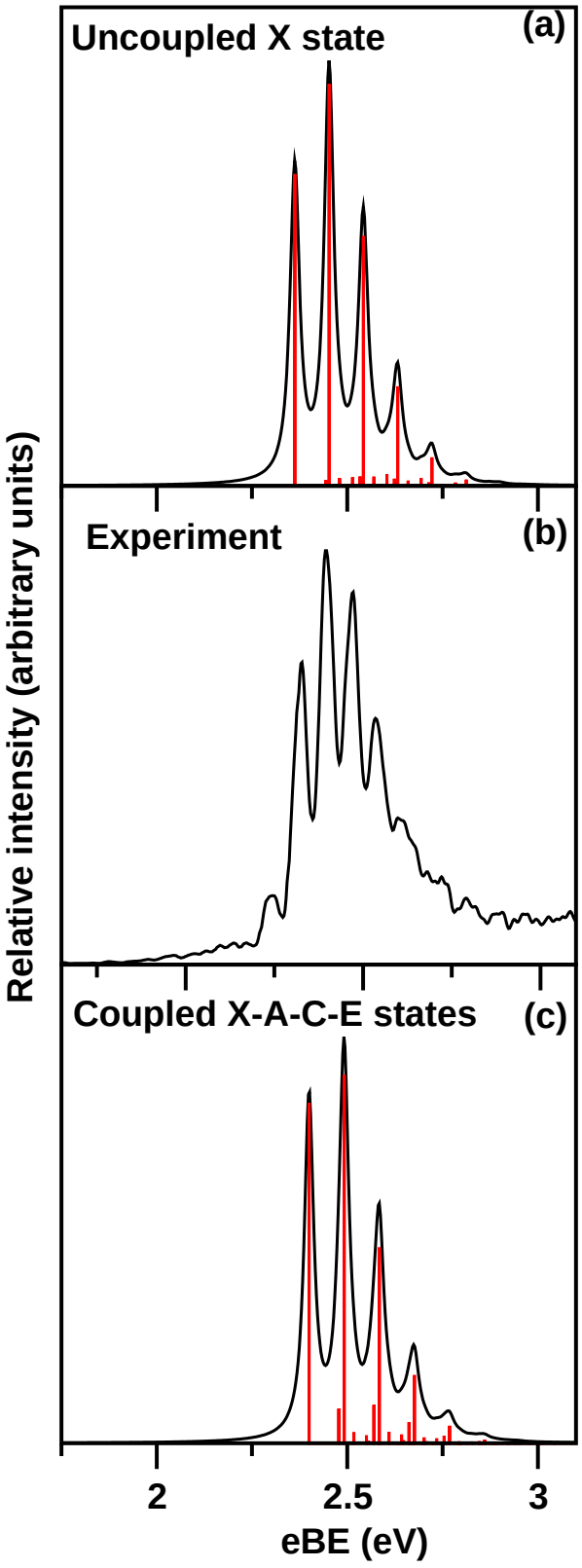

Figure 4.8: Stick vibronic spectrum and convoluted envelope of the $\widetilde{X}^2B_2$ electronic state of B_5 in the uncoupled (panel a) and $\widetilde{X}$-$\widetilde{A}$-$\widetilde{C}$-$\widetilde{E}$ coupled (panel c) states situation. The 355 nm experimental recording reproduced from Ref. [3] and shown in panel b.

symmetry. The coupling strength is strongest between the $\widetilde{X}$ and $\widetilde{C}$ states through the ν_9 vibrational mode. Now considering the data presented in Table 3.34 of Chapter 3 and discussions therein, it is expected that only the $\widetilde{X}$-$\widetilde{A}$ coupling will have some impact on the vibrational structure of the $\widetilde{X}$ band, the intersections of the $\widetilde{X}$ state with the others occur at much higher energies. The coupling effect of each of the above states on the $\widetilde{X}$ band is examined in detail. To save space we do not show the calculated band structures obtained by including each of these couplings. The coupling of the $\widetilde{X}$ state with the rest of the states does not have any major impact on its vibronic structure. The final structure of the $\widetilde{X}$ band including all couplings mentioned above is shown in the panel c of Fig. 4.8. It can be seen that the resolved experimental band structure (panel b) is indeed in good agreement with the theoretical results of panel c and nonadiabatic coupling causes some increase of the vibronic line density. Weak excitations of the nontotally symmetric coupling vibrational modes ν_7, ν_8 and ν_9 are extracted from the stick vibronic spectrum of panel c.

The vibrational structure of the uncoupled $\widetilde{A}$ state of B_5 is presented in panel a along with the better resolved 266 nm experimental recording [3] in panel b of Fig. 4.9. It can be seen that the overall structure of the theoretical band is already in good agreement with the experimental results. All symmetric vibrational modes are very weakly active (cf., Table 3.25 of Chapter 3) in this electronic state. The excitation strength of the ν_4 vibrational mode is highest among them. We indeed find the progression of ν_4 vibrational mode with an energy spacings of ~ 530 cm^{-1} in theoretical stick spectrum of Fig 4.9(a). An energy spacing of ~ 530 cm^{-1} similar to that in the $\widetilde{X}$ band was reported in the experiment [3]. We note that we differ with the experiment [3] in terms of major progressions in the $\widetilde{X}$ and $\widetilde{A}$ bands of B_5. The theory predicts major progression of ν_3 in the $\widetilde{X}$ and ν_4 in the $\widetilde{A}$ state of B_5.

The equilibrium minimum of the $\widetilde{A}$ state occurs ~ 0.6 and ~ 0.7 eV below the minimum of the $\widetilde{X}$-$\widetilde{A}$ and $\widetilde{A}$-$\widetilde{B}$ CIs (see Chapter 3 for details). These two pairs of states are coupled by the vibrational modes ν_7, ν_9 and ν_7 (cf., Table 3.26 of Chapter 3), respectively. The vibronic structure of the $\widetilde{A}$ state obtained by including the coupling with the $\widetilde{X}$ and $\widetilde{B}$ states is shown in panel c of Fig. 4.9. It can be seen from the latter that the nonadiabatic coupling causes an increase of the spectral line density although the intensity of the lines is very small. As a result the spectral envelope becomes broad and diffuse and agrees more closely to the experiment. Weak excitation of ν_9 vibrational mode is found in this case.

Although a partially structured $\widetilde{B}$ band with extremely low intensity was obtained in the 266 nm recording it appeared to be very broad and diffuse in the 193 nm recording [3]. No vibrational progressions could be resolved from these experimental band structures. The data of Table 3.26 of Chapter 3 reveal that the $\widetilde{B}$ state is coupled (in first-order) with $\widetilde{A}$, $\widetilde{C}$ and $\widetilde{E}$ electronic states via the vibrational modes ν_8; ν_8, ν_9 and ν_7, ν_9, respectively, of b_2 symmetry. The equilibrium minimum of the $\widetilde{B}$ state occurs ~ 0.06, ~ 1.58 and ~ 4.90 eV below the minimum of the $\widetilde{A}$-$\widetilde{B}$, $\widetilde{B}$-$\widetilde{C}$ and $\widetilde{B}$-$\widetilde{E}$ CIs. It therefore appears to be interesting to critically investigate the impact of these couplings on the observed diffuse structure of the $\widetilde{B}$ band of B_5.

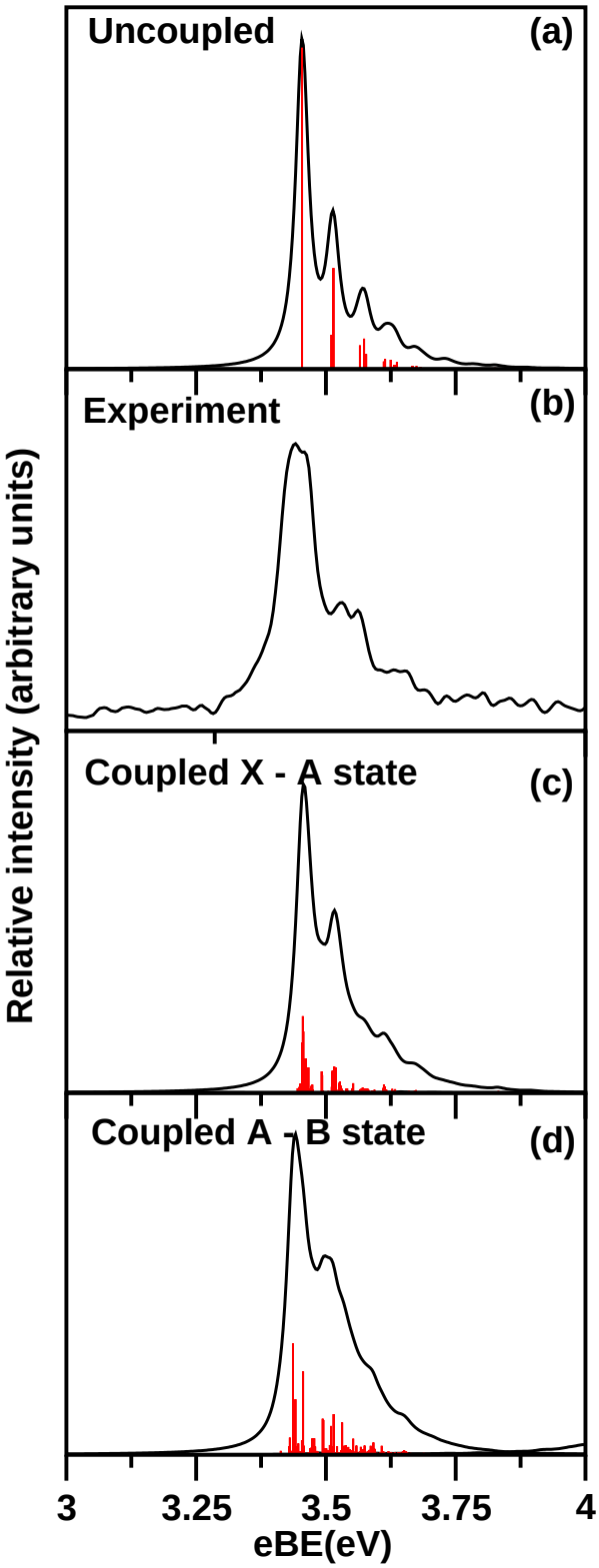

Figure 4.9: Same as in Fig. 4.8 for the $\widetilde{A}^2A_1$ electronic state of B_5 in the uncoupled (panel a) and coupled (panel c) states situations. The 266 nm experimental recording of Ref. [3] is reproduced in panel b.

The vibrational structure of the uncoupled $\widetilde{B}$ state is presented in panel a of Fig. 4.10. All four totally symmetric vibrational modes are excited in this band. The excitation of the mode ν_3 is strongest. Peak spacings of 1242, 901, 723 and 337 cm^{-1} corresponding to the modified frequency of ν_1, ν_2, ν_3 and ν_4 vibrational modes, respectively, in the $\widetilde{B}$ state are extracted from the stick line spectrum of Fig. 4.10(a). The $\widetilde{B}$ band is examined by including the $\widetilde{A}$-$\widetilde{B}$, $\widetilde{B}$-$\widetilde{C}$ and $\widetilde{B}$-$\widetilde{E}$ couplings. The effect of $\widetilde{A}$-$\widetilde{B}$ coupling on the structure of the $\widetilde{B}$ band is found to be the strongest. It causes a huge increase in the vibronic line density. As mentioned above that the $\widetilde{B}$ state minimum occurs only ~ 0.06 eV below the minimum of the $\widetilde{A}$-$\widetilde{B}$ CIs and therefore the entire $\widetilde{B}$ band is perturbed by the associated nonadiabatic coupling. In contrast, the effect of coupling with the $\widetilde{C}$ and $\widetilde{E}$ states on the structure of the $\widetilde{B}$ band is far less. The $\widetilde{B}$ band obtained by including the above couplings is shown in panel c of Fig. 4.10. It can be seen that observed diffuse structure of this band [3] is much better reproduced by the spectrum of panel c.

The vibrational energy level spectrum of the uncoupled $\widetilde{C}$, $\widetilde{D}$ and $\widetilde{E}$ electronic states are shown in panel a, b and c, respectively, of Fig. 4.11. The vibrational modes ν_1 and ν_4 form detectable progression in the $\widetilde{C}$ state. Line spacings of ~ 1191 and ~ 474 cm^{-1}, respectively, are extracted from the spectrum of the $\widetilde{C}$ state. The vibrational mode ν_2 form extended progression in the $\widetilde{D}$ state. Line spacing of ~ 964 cm^{-1} has been found from its spectrum shown in panel b. The vibrational modes ν_1, ν_3 and ν_4 from detectable progression in the spectrum of the $\widetilde{E}$ state shown in Fig. 4.11(c). Peak spacings of 1239, 723 and 471 cm^{-1} corresponding to the excitation of these modes, respectively, are extracted from this spectrum.

It is discussed in Chapter 3 that the $\widetilde{C}$ state is coupled with the $\widetilde{X}$ and $\widetilde{B}$ states, the $\widetilde{D}$ state is coupled with the $\widetilde{E}$ state and the $\widetilde{E}$ state is coupled with the $\widetilde{X}$, $\widetilde{B}$ and $\widetilde{D}$ states. The $\widetilde{D}$-$\widetilde{E}$, $\widetilde{B}$-$\widetilde{E}$ and $\widetilde{X}$-$\widetilde{E}$ couplings are quite strong. The equilibrium minimum of the $\widetilde{E}$ state is quasi-degenerate with the energetic minimum of the seam of $\widetilde{D}$-$\widetilde{E}$ CIs. The $\widetilde{X}$-$\widetilde{E}$ and $\widetilde{B}$-$\widetilde{E}$ CIs occur at much higher energies and are not relevant in the energy range of the $\widetilde{E}$ band. A similar consideration on energetic ground reveals that the $\widetilde{B}$-$\widetilde{C}$, $\widetilde{C}$-$\widetilde{D}$, $\widetilde{B}$-$\widetilde{D}$ CIs will play important role in the vibronic structure of the $\widetilde{C}$ and $\widetilde{D}$ bands. The band structures of the $\widetilde{C}$, $\widetilde{D}$ and $\widetilde{E}$ electronic states obtained by including the couplings mentioned above are shown in the panel a, b and c of Fig. 4.12, respectively. While the impact of these couplings is not very significant on the $\widetilde{C}$ and $\widetilde{D}$ bands, the structure of the $\widetilde{E}$ band is considerably modified by them.

Internal conversion dynamics

Similar to the case of neutral electronic states of B_4^-, the time-dependence of electronic population of the neutral electronic states of B_5 is recorded, when the WP prepared on $\widetilde{X}$, $\widetilde{A}$, $\widetilde{B}$, $\widetilde{C}$, $\widetilde{D}$ and $\widetilde{E}$ electronic states and is plotted in panels a-f of Fig. 4.13. From the figure, it can be seen that no major flow of electronic population takes place to the other states when the WP is initially prepared on the $\widetilde{X}$, $\widetilde{A}$, $\widetilde{C}$ and $\widetilde{D}$ electronic states. In contrast, the electron population dynamics is quite involved for an initial location of the WP either on the $\widetilde{B}$ and $\widetilde{E}$ electronic states. The latter two cases are shown in panel a and b of Fig. 4.14, respectively. The decay and growth of adiabatic (thick solid line) and

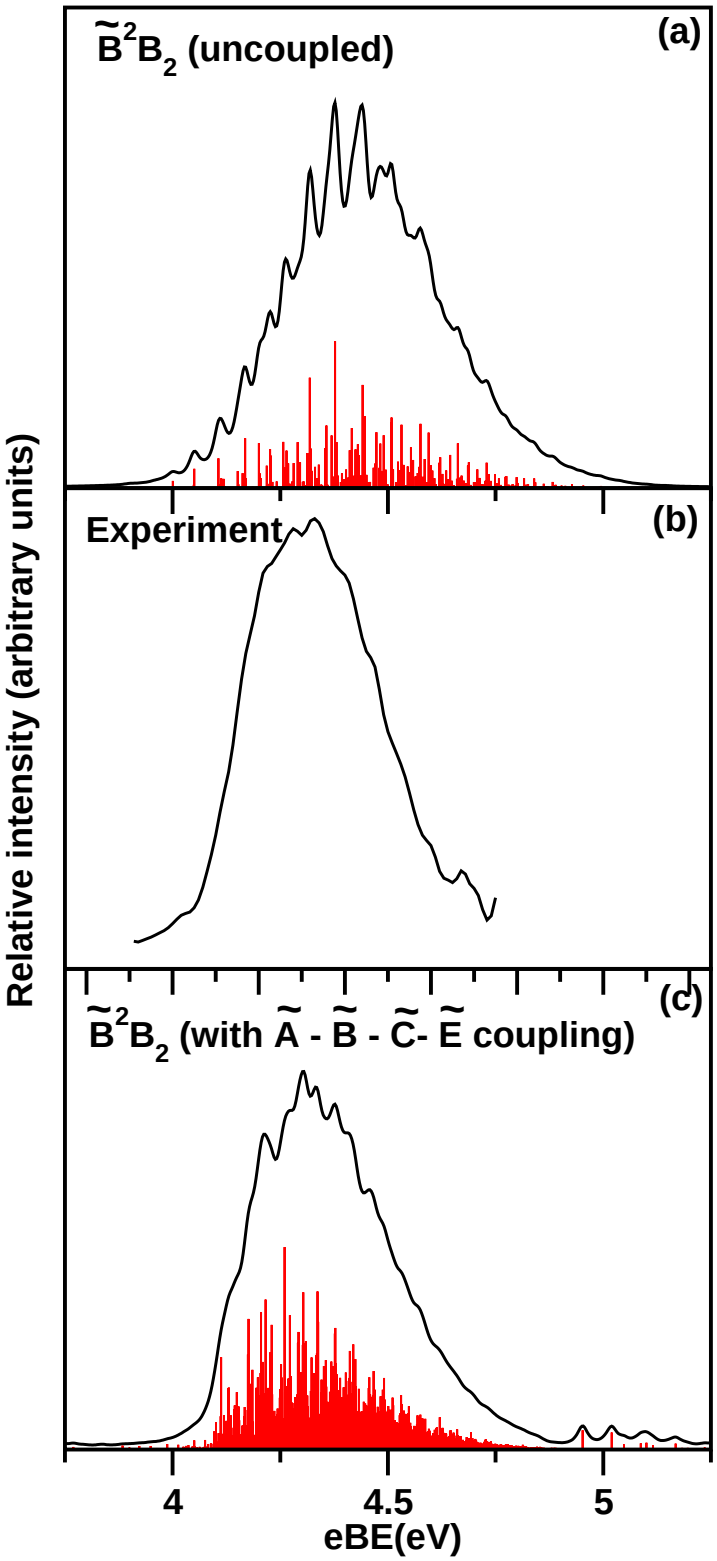

Figure 4.10: Same as in Fig. 4.8 for the $\widetilde{B}^2B_2$ state of B_5. The $\widetilde{B}$ band obtained in the uncoupled and coupled ($\widetilde{A}$-$\widetilde{B}$-$\widetilde{C}$-$\widetilde{E}$) states situations is shown in panel a and c, respectively. The 193 nm experimental recording is reproduced from Ref. [3] and shown in panel b.

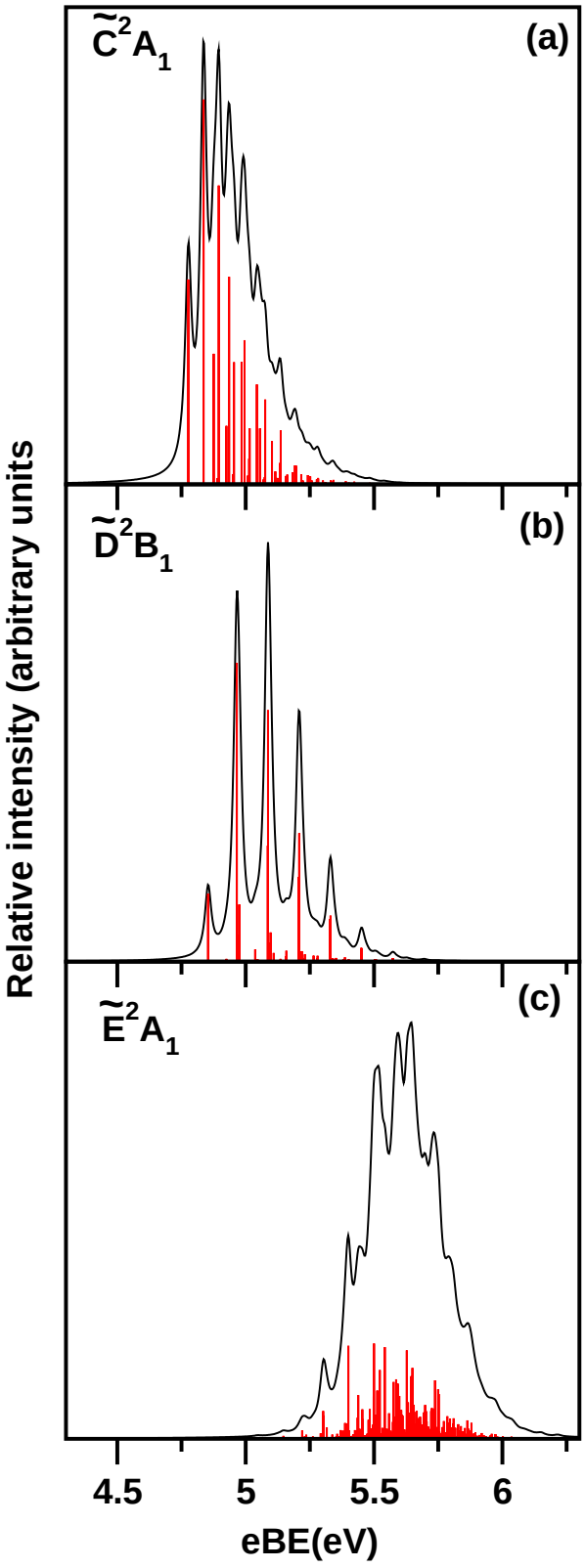

Figure 4.11: Same as in Fig. 4.8 for the uncoupled $\widetilde{C}^2A_1$, $\widetilde{D}^2B_1$ and $\widetilde{E}^2A_1$ electronic states of B_5.

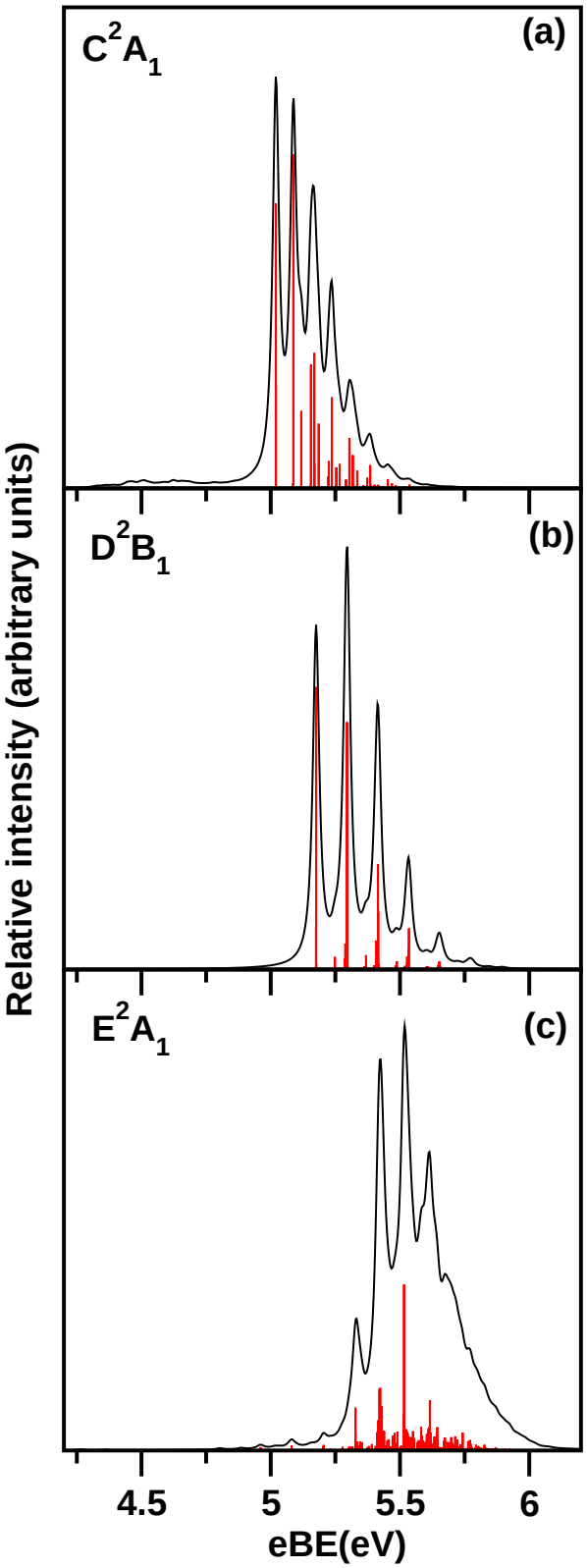

Figure 4.12: The same $\widetilde{C}^2A_1$, $\widetilde{D}^2B_1$ and $\widetilde{E}^2A_1$ states in fully coupled situation is shown in panel a, b and c respectively. These simulations were done by MCTDH diagonalization procedure.

diabatic (thin dashed line) electronic populations for an initial location of the WP on the $\widetilde{B}$ state are plotted in panel a of Fig. 4.14. The $\widetilde{B}$ states population starts from 1.0 (diabatic) and 0.96 (adiabatic) at t=0 and rapidly decays to the $\widetilde{A}$ state and relatively slowly to the $\widetilde{X}$ state in time. This is indicated by the growth of populations of the latter two states. The decay of the $\widetilde{B}$ state population is much faster in the adiabatic picture and relates to a decay rate of $\sim$ 12 fs (adiabatic) and $\sim$ 38 fs (diabatic). The coupling between the $\widetilde{A}$-$\widetilde{B}$ state caused by the ν_8 vibrational mode of b_2 symmetry. Although the strength of this coupling is not very large [cf., Table 3.34 of Chapter 3], the energetic minimum of the $\widetilde{B}$ state located only $\sim$ 0.06 eV below the minimum of the $\widetilde{A}$-$\widetilde{B}$ CIs. This causes a fairly strong mixing of the lower vibrational levels of the $\widetilde{B}$ states with higher vibrational levels of $\widetilde{A}$ state and a huge increase of the vibronic line density of the $\widetilde{B}$ state starting from its adiabatic detachment position [cf., Fig. 4.10(c)]. The adiabatic population of the $\widetilde{B}$ state exhibits damped oscillations and saturates at $\sim$ 0.2 at longer time. The damping of the oscillations caused by the strong anharmonicity by the WP in the vicinity of the CIs during its evolution. These quasiperiodic oscillations reveal a period of 36 fs which roughly corresponds to the frequency of the ν_2 vibrational mode. The $\widetilde{B}$ state is not directly coupled to the $\widetilde{X}$ state of B_5. However the small population flow to the $\widetilde{X}$ state seen in panel a of Fig. 4.14 is mediated via the $\widetilde{X}$-$\widetilde{A}$ CIs. It can be seen that within about 10 fs the population start flowing to the $\widetilde{X}$ state indicating an extremely fast internal conversion dynamics. The population of the $\widetilde{X}$ state saturates roughly to the same value as of the $\widetilde{B}$ state at longer time.

Except the $\widetilde{X}$ state the electron population flows to all excited states when the WP is initially prepared on the $\widetilde{E}$ state as can be seen from panel b of Fig. 4.14. The adiabatic population of the $\widetilde{E}$ state decays much faster (in about $\sim$ 12 fs) compared to its diabatic population ($\sim$ 167 fs). The $\widetilde{E}$ state quickly relaxes to the $\widetilde{D}$ state as its equilibrium minimum is quasi-degenerate with the minimum of the $\widetilde{D}$-$\widetilde{E}$ CIs. The damped recurrences in the adiabatic populations of the $\widetilde{D}$ and $\widetilde{E}$ electronic states occur in a period of $\sim$ 26 fs which correlates to the vibrational period of the ν_1 mode. The $\widetilde{X}$-$\widetilde{E}$ CIs occur at higher energies ($\sim$ 2.01 eV above the $\widetilde{E}$ state minimum) and therefore no direct population transfer to the $\widetilde{X}$ state can be seen. The population can however, directly flow to the $\widetilde{B}$ state through the $\widetilde{B}$-$\widetilde{E}$ CIs. The small population flow to the $\widetilde{A}$ and $\widetilde{C}$ states occurs indirectly through the $\widetilde{A}$-$\widetilde{B}$ and $\widetilde{B}$-$\widetilde{C}$ CIs, respectively.

4.2.3 Photodetachment bands of B_7^-

In this section we present and discuss the photodetachment bands of B_7^- originating from its three isomers discussed above. Theoretical results are compared with the experimental band structures and assigned. Wang and co-workers [4] assigned origin of the observed peaks X and D to isomer I, X, E, F, H and I to isomer II and A, B and G to isomer III (*cf.* panel a of Fig. 4.20 and Table 3.15) by performing extensive quantum chemistry calculations of VDEs. In the following, the detachment bands are calculated by employing the vibronic Hamiltonians $\mathcal{H}_{\rm I}$, $\mathcal{H}_{\rm II}$ and $\mathcal{H}_{\rm III}$ developed in section 3.3.3 and both by time-independent and time-dependent quantum mechanical methods. In

the former approach the Hamiltonian matrix is represented in a direct product harmonic oscillator basis of relevant vibrational modes and then diagonalized with the aid of Lanczos algorithm [18] to calculate the precise location of the vibronic eigenvalues. The spectral intensity is calculated by the golden rule equation. In the time-dependent approach WP pertinent to reference initial state of the anion is propagated on the coupled manifold of electronic states of the neutral isomer. At each step of propagation the time autocorrelation function is calculated. The latter is Fourier transformed to calculate the broad band detachment spectrum. The decay of the excited electronic states of the neutral cluster is studied by recording the time-dependence of the electronic population. The WP propagation is carried out within the framework of MCTDH approach employing the Heidelberg MCTDH suite of programs [14–17]. The assignment of the peaks observed in the experimental spectrum (*cf.* Fig. 4.20) in terms of VDEs agrees quite well with our estimate of the same (*cf.* Table 3.15). Therefore, in the remaining of this section we have undertaken the exercise to analyze the details of each of these peaks (rather bands) and discuss the nuclear dynamics on the relevant electronic states of the corresponding neutral isomer. Several reduced dimensional calculations are performed in order to detect the progression of the vibrational modes in each band. To save space the details of this exercise is not presented here for brevity, however, the important findings are discussed and related to the broad and overlapping structure of each band recorded in the experiment. To this effort the vibronic structure of the mentioned electronic states of each of the isomer is first presented and discussed. The overall composite band structure is presented in a later section and compared with experimental results.

Vibronic structure of the electronic states of isomer I

The three degenerate electronic states of the isomer I are JT active. In the absence of intermode bilinear couplings the vibronic Hamiltonian of each of these states is separable in terms of the symmetric a_1 and JT active degenerate e_2 vibrational modes. Therefore, partial spectra considering these modes are calculated separately by the time-independent method. Analysis of these spectra facilitates the assignment of dominant vibrational progression in the final band structure calculated including all relevant couplings among electronic states and vibrational modes. To save space and for brevity we do not show all partial spectra here however, the important finding are discussed below.

The partial spectrum of the symmetric vibrational modes revealed dominant progression of ν_2 vibrational mode in the $\widetilde{X}$ state. This mode is strongly Condon active in this state (*cf.* Table 3.28). The energetic minimum of the $\widetilde{X}$ state shifts considerable away (by $Q_2 = \sim 3.68$) from the reference equilibrium geometry at Q_2=0 along this mode [*cf.* Fig. 3.18 (b)]. As a result, the center-of-gravity of this partial spectrum occurs at the position of the sixth quantum of excitation of this mode. Line spacings of $\sim$206 cm^{-1} corresponding to the frequency of ν_2 vibrational mode is extracted from the spectrum. The vibrational mode ν_1 is very weakly excited in this state. Similar partial spectra of the $\widetilde{A}$ and $\widetilde{B}$ states reveal negligible excitations of the vibrational modes ν_1 and ν_2 in these states.

The vibrational modes of e_2 symmetry are JT active in the $\widetilde{X}$, $\widetilde{A}$ and $\widetilde{B}$ electronic

Table 4.6: The number of HO basis functions used in the calculation of the stick vibronic spectrum of the mentioned electronic states of neutral isomer I of B_7.

State(s)	Lanczos iterations	No. of HO basis ν_1,ν_2,ν_{8x},ν_{8y},ν_{9x},ν_{9y},ν_{10x},ν_{10y}	Figure number
$\widetilde{X}^2E_1$	5000	8, 40, 12, 12, 6, 6, 20, 20	Fig. 4.15(a)
$\widetilde{A}^4E_1$	5000	25, 10, 20, 20, 6, 6, 12, 12	Fig. 4.15(b)
$\widetilde{B}^2E_1$	5000	30, 10, 15, 15, 6, 6, 15, 15	Fig. 4.15(c)

states. The partial spectra of these modes reveal irregular vibronic structures of all three states. As a result of the JT effect the vibronic levels of the upper and lower adiabatic component of the JT split states mix. Such mixing transforms the discrete vibronic lines to a cluster of lines involving quasi bound resonances. A careful examination reveals that the vibrational mode ν_{10} is the most active JT mode in the $\widetilde{X}$ state and line spacing of $\sim$477 cm^{-1} is extracted from the JT spectrum of this state. The JT activity of this mode is much weaker in the $\widetilde{A}$ and $\widetilde{B}$ states. The JT activity of the vibrational mode ν_9 is the weakest in all three states and that of ν_8 is weak but almost similar in magnitude in all three states discussed above.

The photodetachment bands of all three degenerate states considering all relevant couplings introduced in the Hamiltonian $\mathcal{H}_{\rm I}$ are calculated with the aid of the time-independent matrix diagonalization method. The results are presented in Fig. 4.15, for the $\widetilde{X}$, $\widetilde{A}$ and $\widetilde{B}$ states in panel a, b and c, respectively. The numerical details of the size of the harmonic basis and the number of Lanczos iterations are given in Table 4.6.

The composite band structure of the $\widetilde{X}$ state is shown in panel a reveals discrete line progressions at the lower energies and a huge increase of line density at higher energy. At lower energies below $\sim$2.8 eV the clustering of lines occurs because of mixing of the vibrational modes of a_1 and e_2 symmetry. This region of the spectrum portrays the vibronic structure of the lower adiabatic sheet of the JT split $\widetilde{X}$ state. The JT CI with the upper adiabatic sheet is accessible beyond $\sim$2.77 eV. Therefore, the discrete vibronic levels of the upper adiabatic sheet strongly mix with the quasi-continuum levels of the lower sheet and causes a huge increase of line density beyond this energy as shown in the inset of panel a. A similar explanation holds for the vibronic structure of the $\widetilde{A}$ and $\widetilde{B}$ states plotted in panels b and c, respectively. However, in contrast to the $\widetilde{X}$ state the JT coupling in the $\widetilde{A}$ and $\widetilde{B}$ state is much weaker (*cf.* Table 3.28). Therefore, vibronic line density at higher energies in these latter two bands is much less compared to that in the $\widetilde{X}$ band.

Vibronic structure of the electronic states of isomer II

Within $\sim$6 eV electron binding energy range of the photodetachment spectrum of B_7^- apparently five energetically low-lying electronic states of the neutral isomer II participate. The energies (vertical) of these states are given in Table 3.15. The coupling among these states through vibrational modes of appropriate symmetry is also documented in Table 3.33. It can be seen from the data given in this table that an estimate of the

correct vibronic structure of these electronic state requires simultaneous treatment of nuclear dynamics on the five coupled electronic states. This task could not be accomplished using the matrix diagonalization approach discussed above. This is carried out by propagating WPs using the MCTDH method [14–17] and discussed later in the text. However, as stated earlier in order to assess the progression of vibrational modes in each electronic state and the impact of nonadiabatic coupling on them due to neighboring states, calculations are carried out for uncoupled and various reduced dimensional coupled states situation using the matrix diagonalization approach. The vibronic structures of uncoupled $\widetilde{X}^2B_2$, $\widetilde{A}^2B_1$, $\widetilde{B}^2B_2$, $\widetilde{C}^2A_1$ and $\widetilde{D}^2B_1$ electronic states are presented in panels a-e of Fig. 4.16. The important findings of this exercise are discussed below. Analysis of vibronic structure of each of the above states without including the coupling with their neighbors revealed dominant excitation of the symmetric ν_5 vibrational mode in all of them except in the $\widetilde{C}$ state. Excitation of the ν_4 vibrational mode is stronger in the latter electronic state. Line spacings of $\sim$ 288, $\sim$ 156, $\sim$ 233, $\sim$ 290 and $\sim$ 171 cm^{-1} corresponding to the progression of ν_5 vibrational mode in the $\widetilde{X}$, $\widetilde{A}$, $\widetilde{B}$, $\widetilde{C}$ and $\widetilde{D}$ electronic states, respectively, are extracted from the spectrum of these states. Line spacings of $\sim$ 1116 and $\sim$ 350 cm^{-1} corresponding to the progressions of ν_1 and ν_4 vibrational modes, respectively, are also extracted from the spectrum of the $\widetilde{C}$ state.

The impact of nonadiabatic coupling with the neighboring states on the vibronic structure of a given electronic state is examined next. The numerical details of the calculations are given in Table 4.7. The results are presented in Figs. 4.17 (a-e) for the $\widetilde{X}$, $\widetilde{A}$, $\widetilde{B}$, $\widetilde{C}$ and $\widetilde{D}$ electronic states, respectively. It is found that the band structure of the $\widetilde{X}$ state is mostly perturbed by its coupling with the $\widetilde{A}$ and $\widetilde{C}$ states. Although the coupling strength of the a_2 vibrational modes ν_7 and ν_8 is weak (*cf.* Table 3.33) between the $\widetilde{X}$ and $\widetilde{A}$ states, the energetic minimum of the $\widetilde{X}$-$\widetilde{A}$ intersection is close to the equilibrium minimum of the $\widetilde{X}$ state (*cf.* Table 3.35). Therefore, $\widetilde{X}$-$\widetilde{A}$ coupling has quite some impact on the structure of the $\widetilde{X}$ band. The $\widetilde{X}$ and $\widetilde{C}$ states are strongly coupled by the b_2 vibrational mode ν_{15}. the vibrational mode ν_{14} also makes important contribution to this coupling. The vibronic structure of the $\widetilde{X}$ state by retaining its coupling with the $\widetilde{A}$ and $\widetilde{C}$ states is presented in panel a of Fig. 4.17. The calculated stick vibronic lines are convoluted with a Lorentzian function of $\sim$ 30 meV FWHM to generate the spectral envelope. We note that the same Lorentzian function is used to convolute all stick spectra presented in this chapter. Excitation of nontotally symmetric modes ν_7 and ν_8 with peak spacings of $\sim$665 and $\sim$357 cm^{-1}, respectively, is extracted from the $\widetilde{X}$ state spectrum of Fig. 4.17 (a). The vibronic structure of the $\widetilde{A}$ state is shown in Fig. 4.17 (b) is mostly perturbed by its coupling with the $\widetilde{X}$ state. The energetic minimum of $\widetilde{X}$-$\widetilde{A}$ state intersection occurs only $\sim$0.05 eV above the minimum of the $\widetilde{A}$ state. Unlike the case of $\widetilde{X}$ state, the vibronic structure of $\widetilde{A}$ state is also perturbed by its coupling with the $\widetilde{B}$ state. Excitation of nontotally symmetric modes ν_7 and ν_8 is found in the $\widetilde{A}$ state. The vibronic structure of the $\widetilde{B}$, $\widetilde{C}$ and $\widetilde{D}$ electronic states are shown in panel c, d and e of Fig. 4.17, respectively. Coupling of the $\widetilde{B}$ state with $\widetilde{A}$ and $\widetilde{C}$ states contributes to the vibronic structure of the $\widetilde{B}$ state. Similarly, coupling of the $\widetilde{C}$ state with $\widetilde{B}$ state and $\widetilde{D}$ state with $\widetilde{C}$ state contributes to their

Table 4.7: The number of harmonic oscillator basis function used in the calculation of the stick vibronic spectrum of the mentioned electronic states of neutral isomer II of B_7.

State(s)	Laczos iterations	No. of HO basis along symmetric modes ν_1-ν_5	coupling modes	Figure number
$\widetilde{X}^2B_2$	5000	6, 6, 18, 10, 35		4.16(a)
$\widetilde{A}^2B_1$	5000	6, 18, 6, 15, 30		4.16(b)
$\widetilde{B}^2B_2$	5000	18, 6, 6, 12, 40		4.16(c)
$\widetilde{C}^2A_1$	5000	30, 15, 6, 30, 15		4.16(d)
$\widetilde{D}^2B_1$	5000	6, 6, 15, 6, 30		4.16(e)
$\widetilde{X}^2B_2$ -$\widetilde{A}^2B_1$	5000	10, 6, 15, 6, 25	6 (ν_6), 10 (ν_7), 6 (ν_8)	Fig. 4.17(a)
$\widetilde{X}^2B_2$ -$\widetilde{C}^2A_1$	5000	10, 6, 4, 10, 6	6 (ν_{12}), 6 (ν_{13}), 8 (ν_{14}), 10 (ν_{15})	
$\widetilde{X}^2B_2$ -$\widetilde{D}^2B_1$	5000	6, 6, 10, 6, 20	4 (ν_6), 10 (ν_7), 8 (ν_8)	
$\widetilde{A}^2B_1$ -$\widetilde{B}^2B_2$	5000	8, 4, 8, 6, 15	6 (ν_6), 6 (ν_7), 6 (ν_8)	Fig. 4.17(b)
$\widetilde{A}^2B_1$ -$\widetilde{C}^2A_1$	5000	8, 6, 4, 8, 10	4 (ν_9), 4 (ν_{10}), 8 (ν_{11})	
$\widetilde{B}^2B_2$ -$\widetilde{C}^2A_1$	5000	25, 8, 4, 25, 10	4 (ν_{12}), 8 (ν_{13}), 6 (ν_{14}), 15 (ν_{15})	Fig. 4.17(c)
$\widetilde{B}^2B_2$ -$\widetilde{D}^2B_1$	5000	4, 4, 8, 6, 15	4 (ν_6), 8 (ν_7), 4 (ν_8)	
$\widetilde{C}^2A_1$ -$\widetilde{D}^2B_1$	5000	6, 6, 10, 6, 20	6 (ν_9), 10 (ν_{10}), 6 (ν_{11})	Fig. 4.17(d & e)

respective vibronic structure. The vibrational mode ν_{15} of b_2 symmetry strongly couples to $\widetilde{B}$ and $\widetilde{C}$ electronic states and the minimum of the $\widetilde{B}$ and $\widetilde{C}$ intersections is closer to their respective equilibrium minimum (*cf.* Table 3.35). In addition, the $\widetilde{B}$ state is also strongly coupled with the $\widetilde{D}$ state. As a result, its vibronic structure is strongly perturbed by the associated nonadiabatic coupling. Excitations of nontotally symmetric modes ν_8 & ν_{15}, ν_{14} & ν_{15} and ν_7 are found from the spectrum of the $\widetilde{B}$, $\widetilde{C}$ and $\widetilde{D}$ state, respectively.

Vibronic structure of the electronic states of isomer III

The vibronic structure of the $^2A_2$, $^2B_2$, $\widetilde{B'}^2B_1$, $\widetilde{C'}^2A_1$ and $\widetilde{D'}^2A_1$ electronic states is similarly examined as discussed in sections 4.2.3 and 4.2.3 above. While the vibronic structures of uncoupled $^2A_2$, $^2B_2$, $\widetilde{B'}^2B_1$, $\widetilde{C'}^2A_1$ and $\widetilde{D'}^2A_1$ electronic states are presented in Fig. 4.18, the same including the most relevant interstate couplings are shown in Fig. 4.19 (panel a: $^2A_2$, b: $^2B_2$, c: $\widetilde{B'}^2B_1$, d: $\widetilde{C'}^2A_1$, e: $\widetilde{D'}^2A_1$). The coupling schemes as well as the numerical details of the calculations are given in Table 4.8. In comparison with Fig. 4.17, it can be seen that the nonadiabatic coupling effects are generally stronger in the electronic states of isomer III. In contrast to the assignment of Boldyrev and co-workers we find that the A_2 ($\widetilde{X'}$) state is lower in energy than the B_2 ($\widetilde{A'}$) state at the vertical configuration. This aspect is explicitly confirmed by varying the size of the basis set and the active space in the CASSCF/MRCI calculations. A detail comparison with the experimental band structure is discussed in the subsequent section.

A careful examination of various spectra presented in Figs. 4.18 (a-e) and also corresponding uncoupled state spectra reveal the following. The symmetric vibrational modes ν_1 and ν_6 form dominant progression in the $\widetilde{X'}$, $\widetilde{A'}$, $\widetilde{B'}$, $\widetilde{C'}$ and $\widetilde{D'}$ electronic states. Peak spacings of 1331 & 354, 1411 & 301, 1535 & 409, 1280 & 323 and 1337 & 440 cm^{-1} due to ν_1 & ν_6 vibrational modes are found in the vibronic structure of the above states, in that order. The excitation of the mode ν_1 and ν_6 is strongest in the and $\widetilde{C'}$ and $\widetilde{D'}$ states, respectively. The excitation of the remaining symmetric vibrational modes is

Table 4.8: The same data as Tables 4.7 for neutral isomer III of B_7.

State(s)	Lanczos iterations	No. of HO basis: Symmetric modes ν_1-ν_6	No. of HO basis: Coupling modes	Figure numbers
$^2A_2$	5000	20, 8, 8, 8, 20		4.18(a)
$^2B_2$	5000	4, 20, 4, 20, 10, 20		4.18(b)
$\widetilde{B'}^2B_1$	5000	25, 12, 6, 6, 6, 20		4.18(c)
$\widetilde{C'}^2A_1$	5000	20, 12, 6, 6, 6, 40		4.18(d)
$\widetilde{D'}^2A_1$	5000	40, 4, 18, 4, 4, 18		4.18(e)
$^2A_2$ -$^2B_2$	5000	10, 4, 4, 4, 4, 10	6(ν_9), 10 (ν_{10})	Fig. 4.19(a & b)
$^2A_2$ -$\widetilde{B'}^2B_1$	5000	10, 4, 6, 4, 20	0 (ν_{11}), 6 (ν_{12}), 0 (ν_{13}), 0 (ν_{14}), 0 (ν_{15})	
$^2A_2$ -$\widetilde{C'}^2A_1$	5000	10, 6, 4, 6, 4, 15	8 (ν_7), 4 (ν_8)	
$^2A_2$ -$\widetilde{D'}^2A_1$	5000	25, 4, 10, 4, 4, 15	4 (ν_7), 4 (ν_8)	
$^2B_2$ -$\widetilde{C'}^2A_1$	5000	18, 4, 4, 4, 8, 20	6(ν_{11}), 6 (ν_{12}), 0 (ν_{13}), 0 (ν_{14}), 0 (ν_{15})	
$^2B_2$ -$\widetilde{D'}^2A_1$	5000	15, 4, 8, 4, 4, 10	6(ν_{11}), 0 (ν_{12}), 6 (ν_{13}), 8 (ν_{14}), 0 (ν_{15})	
$\widetilde{B'}^2B_1$ -$\widetilde{C'}^2A_1$	5000	10, 6, 4, 4, 4, 10	6 (ν_9), 8 (ν_{10})	Fig. 4.19(c)
$\widetilde{B'}^2B_1$ -$\widetilde{D'}^2A_1$	5000	10, 6, 6, 4, 4, 10	8 (ν_9), 8 (ν_{10})	
$\widetilde{C'}^2A_1$ -$\widetilde{D'}^2A_1$	5000	30, 6, 6, 15, 6, 30		Fig. 4.19(d & e)

weaker in these states. All symmetric vibrational modes are very weakly excited in the $\widetilde{A'}$ state. The impact of the $\widetilde{X'}$-$\widetilde{A'}$ coupling on the vibronic structure of the $\widetilde{X'}$ band [*cf.* Fig. 4.19 (a)] is strongest. This coupling is mainly caused by the ν_{10} vibrational mode of b_1 symmetry. Although the $\widetilde{X'}$ and $\widetilde{C'}$ states are fairly strongly coupled through ν_7 vibrational mode of a_2 symmetry (*cf.* Table 3.33), impact of this coupling on the structure of $\widetilde{X'}$ band is not as profound as due to the $\widetilde{A'}$ state. This is because the energetic minimum of the $\widetilde{X'}$-$\widetilde{C'}$ CIs occurs at much higher energy compared to that of the $\widetilde{X'}$-$\widetilde{A'}$ states. Excitation of nontotally symmetric vibrational modes ν_8 and ν_{10} are found in the $\widetilde{X'}$ band of Fig, 4.19. Peak spacings of ∼245 and ∼131 cm^{-1} due to the above vibrational modes are extracted from the spectrum. The coupling parameters recorded in Table 3.33 reveal that the vibronic structure of the $\widetilde{A'}$ state is perturbed mostly by its coupling with the $\widetilde{X'}$ state. Likewise, $\widetilde{B'}$-$\widetilde{C'}$ coupling mutually perturbs their vibronic structures. In addition, coupling of the $\widetilde{C'}$ state with $\widetilde{X'}$ state also makes significant contributions to the structure of the $\widetilde{C'}$ state. Vibronic structure of the $\widetilde{D'}$ state is mainly perturbed by its coupling with the $\widetilde{A'}$ and $\widetilde{B'}$ states. Although the $\widetilde{C'}$ state has negligible contribution to the structure of the $\widetilde{X'}$ state, its energetic minimum is quasi-degenerate with the minimum of the $\widetilde{X'}$-$\widetilde{C'}$ intersections (*cf.* Table 3.35). As a result $\widetilde{X'}$-$\widetilde{C'}$ coupling through ν_7 vibrational mode of a_2 symmetry makes significant contribution to the vibronic structure of the $\widetilde{C'}$ state. Excitation of nontotally symmetric modes ν_{10}, ν_9 & ν_{10}, ν_7 & ν_{10} and ν_{10} & ν_{14} are found in the $\widetilde{A'}$, $\widetilde{B'}$, $\widetilde{C'}$ and $\widetilde{D'}$ states, respectively.

Composite photodetachment bands versus experiment

The photodetachment bands of all three isomers are calculated separately employing the full Hamiltonians ($\mathcal{H}_{\rm I}$, $\mathcal{H}_{\rm II}$ and $\mathcal{H}_{\rm III}$) and WP propagation method. The MCTDH suite of programs is used for this purpose [14–17]. For each isomer separate calculations are carried out for six different initial locations of the WP. The resulting time autocorrelation functions are then combined and damped with an exponential function ($e^{-\frac{t}{\tau}}$, with τ=33 fs) to generate the broad band spectral envelope. The technical details of the calculations for each isomer are given in Table 4.9. The spectral envelopes of three isomers are plotted

separately in panel b of Fig. 4.20 and shown by black (isomer I), red (isomer II) and blue (isomer III) color lines. The composite theoretical band structure of all three isomers is shown in panel c. The 193 nm experimental recording of Ref. [4] is shown in panel a. As mentioned in the introduction, eleven distinct peaks are identified in the experiment by recording the detachment spectrum with 355, 266 and 193 nm laser photon. These peaks are assigned by calculating the VDEs [4] as illustrated in Table 3.15. The origin of the theoretical spectra plotted in panel b and c is placed at the experimental adiabatic ionization energies reported in Ref. [4].

A careful inspection of the theoretical and experimental results shown in Fig. 4.20 reveal the following. The broad threshold feature representing the X band originates from both isomer I and II. The A, B, C and G bands originate from isomer III. It is mentioned before that a very sharp band with a short progression of ∼480 (40) cm^{-1} was observed in the experiment [4]. This band is identified with the vibronic structure of the $^2B_2$ electronic state of the neutral isomer III supported by the VDE data calculated by the OVGF method [4]. The VDE data calculated by us by the same method also supports this assignment. The very sharp structure of this band is attributed to very small geometry changes of the neutral B_7 in the $^2B_2$ state as compared to the geometry of the electronic ground state of the anionic isomer III. An adiabatic detachment energy of ∼3.44(2) eV is estimated for this band from the experimental data [4]. As discussed in Sec. 4.2.3 and noted in Table 3.15 that the CASSCF-MRCI calculations yield a reverse energetic ordering of the $^2B_2$ and $^2A_2$ electronic states of the neutral isomer III. According to the latter results, the $^2A_2$ state is the electronic ground state of this isomer. Now a close look at the vibronic energy level structure of the $^2A_2$ [Fig. 4.19(a)] and $^2B_2$ [Fig. 4.19(b)] states of the neutral isomer III clearly indicates that the latter structure closely resembles the structure of the observed band A. A short vibronic progression of ∼460 cm^{-1} can also be observed from the band structure of Fig. 4.19(b) in excellent agreement with the experiment. This progression can be attributed to both ν_4 and ν_5 vibrational modes. These modes have fairly large bilinear coupling (*cf.* Table 3.30). Further to this analysis it can be seen from Fig. 3.21 that the equilibrium minimum of the $^2B_2$ state is more closer to the reference equilibrium minimum (at $\mathbf{Q}$=0) than the $^2A_2$ state. The MO sequence of the anionic isomer III given in Sec. 3.2.3 also suggests that the $^2B_2$ electronic state ought to be the electronic ground state of the corresponding neutral isomer. Therefore, all the evidences furnished above suggest a reverse energetic ordering of the first two electronic states of neutral isomer III of B_7 in the CASSCF-MRCI results. A reversal of this energetic ordering and placing the adiabatic detachment position of the $^2B_2$ state at the reported experimental energy of ∼3.44 eV nicely reproduces the structure of the observed band (*cf.* Fig. 4.20). In contrast, the vibronic spectrum calculated for the coupled $^2B_2$-$^2A_2$ states from the OVGF energy data deviates considerably from the observed band structure of these two electronic states. To support this statement the calculated band structures from the OVGF energy data are given from the OVGF energy data are given panel a ($^2B_2$ state) and b ($^2A_2$ state) of Fig. 4.21. Therefore, the results given above clearly indicates that the CASSCF-MRCI energy data are more accurate for this isomer of B_7 despite a reverse energetic ordering of the first two electronic states. Furthermore, a shakeup

Table 4.9: The normal mode combinations, sizes of the primitive and single particle bases used in the WP propagation (using the MCTDH program modules on the $\widetilde{X}$-$\widetilde{A}$-$\widetilde{B}$ electronic states of neutral isomer I, $\widetilde{X}$, $\widetilde{A}$, $\widetilde{B}$, $\widetilde{C}$ and $\widetilde{D}$ electronic states of neutral isomer II and $\widetilde{X'}$, $\widetilde{A'}$, $\widetilde{B'}$, $\widetilde{C'}$ and $\widetilde{D'}$ electronic states of neutral isomer III of B_7 using Hamiltonians of Eq. 3.10a, 3.11a and 3.11b, respectively.

particle no	Normal modes	SPF basis	Primitive basis
		Isomer I	
1	ν_2, ν_{9x}, ν_{8y}, ν_{7x}	[10,10,8,8,8,8]	(10, 6, 10, 4)
2	ν_1, ν_{8x}, ν_{9y},ν_4	[10,10,8,8,8,8]	(6, 10, 6, 4)
3	ν_{10x}, ν_{10y}, ν_3, ν_5	[10,10,6,6,6,6]	(10, 10, 4, 4)
4	ν_{7y},ν_{6y},ν_{6x}	[6,6,6,6,6,6]	(4, 4, 4)
		Isomer II	
1	ν_5, ν_7, ν_{10}, ν_9, ν_{14}	[20, 10, 15, 10, 10]	(18, 10, 8, 8, 8)
2	ν_4, ν_8 ν_{11}, ν_{12}, ν_{15}	[10, 10, 10, 10, 10]	(8, 10, 8, 8, 8)
3	ν_3, ν_2 ν_1, ν_6, ν_{13}	[15, 10, 15, 10, 10]	(10, 10, 8, 10, 8)
		Isomer III	
1	ν_1,ν_7,ν_{11},ν_{13}	[10, 8, 4, 6]	(6, 6, 10, 8, 4)
2	ν_2,ν_6,ν_{12},ν_{15}	[4, 10, 6, 8]	(4, 8, 16, 4, 12)
3	ν_3,ν_5,ν_9,ν_{14}	[6, 4, 10, 4]	(10, 10, 12, 12, 10)
4	ν_4,ν_8,ν_{10}	[6, 4, 8]	(4, 4, 4, 4, 8)

state at ∼4.14 eV VDE is involved in the higher energy bands of this isomer (see the text below) which cannot be obtained by the OVGF method.

While the location of the C band is missing in the 193 nm experimental spectrum, its existence is clearly seen in the 266 nm experimental spectrum (Fig. 1 of Ref. [4]). The B and C bands originate from the $^2A_2$ electronic state of the neutral isomer III. The $\widetilde{B'}$ state of isomer III, which is a shake-up state is strongly coupled with its $\widetilde{C'}$ and $\widetilde{D'}$ states through the vibrational modes ν_9 and ν_{10} of b_1 symmetry (*cf.* Table 3.33). The broad and diffuse structure of the G band (*cf.* Fig. 4.20) arises from the coupled $\widetilde{B'}$-$\widetilde{C'}$-$\widetilde{D'}$ states of this isomer. The D band represents the vibronic structure of isomer I and originates from its $\widetilde{A}^4E_1$ electronic state. The E, F, H and I bands represent predominantly the vibronic structure of the $\widetilde{A}^2B_1$, $\widetilde{B}^2B_2$, $\widetilde{C}^2A_1$ and $\widetilde{D}^2B_1$ electronic states of isomer II respectively. The separations of G and H bands of ∼ 0.7 eV as found in the experimental results can also be found in the theoretical results (∼ 0.66 eV) of Fig. 4.20 (c). Therefore, it can be concluded that the present theoretical results are on the average in excellent accord with the experimental band structure.

Internal conversion dynamics

Dynamics of the electronic excited states of B_7 clusters is examined in terms of time-dependence of diabatic electronic populations recorded in the WP calculations of Sec.

4.2.3. It is discussed in Sec. 4.2.3 that the three electronically degenerate electronic states of isomer I is JT active and JT effect is strongest in the $\widetilde{X}^2E_1$ electronic state of this isomer. Time-dependence of the populations (diabatic) of the two JT split components of this state is shown in panel a of Fig. 4.22. At time t=0 the population of the component on which the WP is prepared (say component 1) starts from 1.0 and the same for the component 2 is 0.0. It can be seen that population of component 1 transfers to component 2 through the JT CIs.in time and they become equal at = ∼100 fs. At longer time the population of component 2 transfers back to component 1 and fluctuate around a value of ∼0.4. Similar variation of electronic populations of the two components of the $\widetilde{A}^4E_1$ and $\widetilde{B}^2E_1$ states is found. In these cases the JT effect is weak and population transfer occur back and forth between the component states over the entire time interval.

The diabatic electronic populations of the $\widetilde{X}^2B_2$, $\widetilde{A}^2B_1$, $\widetilde{B}^2B_2$, $\widetilde{C}^2A_1$ and $\widetilde{D}^2B_1$ electronic states of neutral isomer II of B_7^- when the WP prepared in $\widetilde{X}$, $\widetilde{A}$, $\widetilde{B}$, $\widetilde{C}$ and $\widetilde{D}$ states are given in panel a, b, c, d and e of Fig. 4.23. When the WP is prepared in $\widetilde{X}$ state, panel a of Fig. 4.23 reveal minor population flow to the other states. The $\widetilde{X}$-$\widetilde{A}$ CI is just ∼0.05 eV above the minimum of $\widetilde{A}$ state (*cf.* Table 3.35). The $\widetilde{X}$-$\widetilde{A}$ CI acts as a funnel for the nonradiative transfer of the $\widetilde{A}$ state to $\widetilde{X}$ state shown in Fig. 4.23(b). As the $\widetilde{X}$ and $\widetilde{A}$ states are well separated from each other and the associated interstate coupling parameter is small, the flow of population expected to be moderate. The other intersections with $\widetilde{A}$ state occurs at much higher energies, and are not expected to create impact on the diabatic population of $\widetilde{A}$ state. The initial population value of the $\widetilde{A}$ state is 1 at t=0. Only 30 % of the population of $\widetilde{A}$ transferred to $\widetilde{X}$ state after 150 fs propagation of the WP, due to the weak coupling with $\widetilde{X}$ state. An initial decay of the population relates to ∼503 fs is estimated from Fig. 4.23(b). Significant population flows to the $\widetilde{A}$ state when the $\widetilde{B}$ state is initially populated (Fig. 4.23 (c)). This happens through the $\widetilde{A}$-$\widetilde{B}$ CIs. From Table 3.35, it can be seen that the $\widetilde{A}$-$\widetilde{B}$ CI minimum is just ∼0.02 eV above the minimum of $\widetilde{B}$ state. Similar situation arises when the WP is initially located on the $\widetilde{C}$ (panel d) and $\widetilde{D}$ (panel e) electronic states. In panel d the $\widetilde{B}$ & $\widetilde{A}$ states populated through $\widetilde{A}$-$\widetilde{C}$ & $\widetilde{B}$-$\widetilde{C}$ CIs, respectively. In panel e $\widetilde{C}$ & $\widetilde{B}$ electronic states populated through $\widetilde{B}$-$\widetilde{D}$ & $\widetilde{C}$-$\widetilde{D}$ CIs, respectively. Nonradiative decay rate of ∼72, ∼136 and ∼86 fs are estimated for $\widetilde{B}$, $\widetilde{C}$ and $\widetilde{D}$ electronic states, respectively.

Similarly, the diabatic populations of the states $^2A_2$, $^2B_2$, $\widetilde{B'}^2B_1$, $\widetilde{C'}^2A_1$ and $\widetilde{D'}^2A_1$ electronic states of neutral isomer III of B_7^- when the WP prepared in $\widetilde{X'}$, $\widetilde{A'}$, $\widetilde{B'}$, $\widetilde{C'}$ and $\widetilde{D'}$ states, are given in panel a, b, c, d and e of Fig. 4.24. The panel a reveals no significant population flow to other states. The population flow from $\widetilde{A'}$, $\widetilde{B'}$, $\widetilde{C'}$ and $\widetilde{D'}$ states through $\widetilde{X'}$-$\widetilde{A'}$, $\widetilde{X'}$-$\widetilde{B'}$, $\widetilde{X'}$-$\widetilde{C'}$ & $\widetilde{B'}$-$\widetilde{C'}$, $\widetilde{C'}$-$\widetilde{D'}$ & $\widetilde{A'}$-$\widetilde{D'}$ CIs can be seen from panels b, c, d and e, respectively. Nonradiative decay rate of ∼89, ∼154, ∼41 and ∼22 fs are estimated for $\widetilde{A'}$, $\widetilde{B'}$, $\widetilde{C'}$ and $\widetilde{D'}$ electronic states, respectively.

4.3 Summary

A theoretical study of the photodetachment spectroscopy of boron cluster anion B_n^- (n=4, 5 and 7) is presented in this chapter. The nuclear dynamics underlying the observed complex structure of the photodetachment bands is studied both by time-independent and time-dependent quantum mechanical methods. The vibronic Hamiltonians developed in Chapter 3 are employed in the investigation. The theoretical results are compared with the experimental findings and discussed in detail.

The nonadiabatic coupling effects are generally found to be small in the photodetachment bands of B_4^-. Some significant effect of such coupling is found in the $\widetilde{a}^3B_{2u}$ and $\widetilde{b}^3B_{1u}$ bands of B_4 only. The symmetric vibrational mode ν_1 and ν_2 forms progression in all the low-lying electronic states of B_4 considered here. The theoretical results are found to be in fair agreement with the experiment and the apparent discrepancy between the two is attributed to the neglect of dynamic spin-orbit coupling in the theoretical treatment and small photodetachment cross sections and inadequate energy resolution in the experiment. In order to confirm that the theoretical results of B_4^- photodetachment do not contain any spin contamination, the equilibrium geometry of B_4^- is optimized both by the UB3LYP and ROMP2 methods (cf., Chapter 3). Using these geometry parameters, two sets of Hamiltonian parameters are derived and dynamics study is performed. Consistent results are obtained in both the cases.

In contrast to B_4^-, the nonadiabatic coupling effects are far more significant in the photodetachment bands of B_5^-. The symmetric vibrational modes ν_3 and ν_4 play most crucial role in this case. Visible impact of nonadiabatic coupling and excitations of nontotally symmetric vibrational modes observed in this case. The complex C band (as designated in the experiment) has been partially described to originate from the $\widetilde{C}^2A_1$, $\widetilde{D}^2B_1$ and $\widetilde{E}^2A_1$ electronic states of B_5. Like the shake-up $\widetilde{E}^2A_1$ state, there are many more states of this kind in the energy range of the C band. A complete analysis of this problem is beyond the scope of the present investigation and will be taken up in future.

Neutral B_7 clusters originating from electron detachment of three isomers (C_{6v} hexagonal pyramidal, C_{2v} pyramidal and C_{2v} planar) of anionic B_7^- cluster are examined and their contribution to the composite experimental band structure is elucidated. The theoretical results are shown to be in good accord with the experimental findings. The impact of the nonadiabatic coupling on the vibronic structure of the photodetachment bands is studied and discussed at length. In addition to totally symmetric vibrational modes excitation of several nontotally symmetric modes is found from the theoretical results. The peaks marked in the experimental spectrum of Fig. 4.20(a) (X to I) are found to originate from the C_{6v} isomer (X and D), pyramidal C_{2v} isomer (X, E, F, H and I) and planar C_{2v} isomer (A, B, C and G). The energetic ordering of the $^2A_2$ and $^2B_2$ states of isomer III is assessed through extensive quantum chemistry calculations and experimental band structures. To the best of our knowledge, B_7 represents a unique system for which the complex vibronic structure of the energetically low-lying electronic state arise from anion precursors of different symmetry and a rich variety of vibronic coupling mechanisms in its energetically low-lying electronic states.

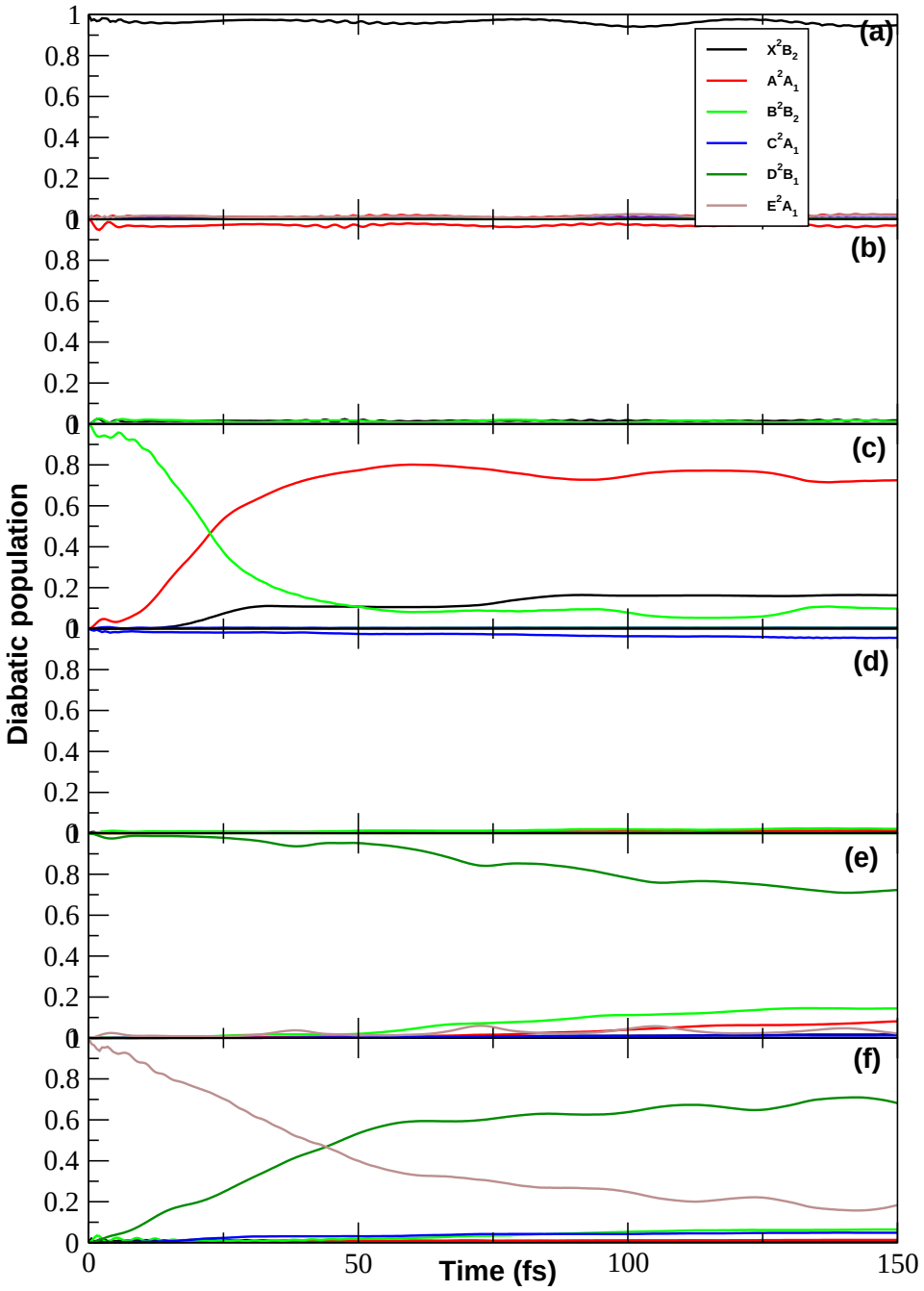

Figure 4.13: Time-dependence of the diabatic electronic populations in the coupled surface dynamics of B_5. The electronic populations for an initial preparation of the WP on the $\widetilde{X}$, $\widetilde{A}$, $\widetilde{B}$, $\widetilde{C}$, $\widetilde{D}$ and $\widetilde{E}$ electronic states are shown in panel a-e, respectively (see text for details).

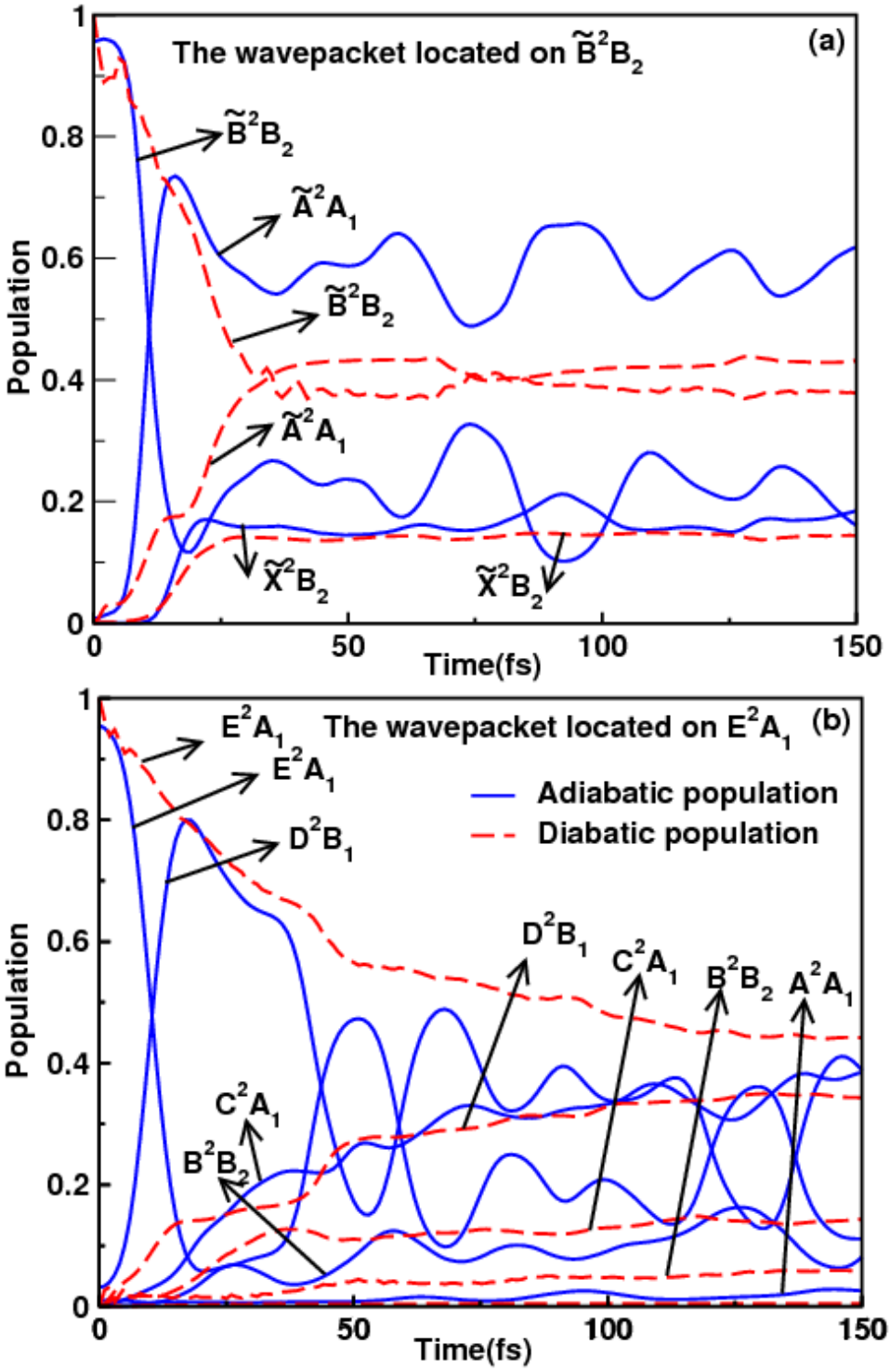

Figure 4.14: Time-dependence of adiabatic (solid lines) and diabatic(dashed lines) for an initial location of the WP on the $\widetilde{B}^2B_2$ (panel a) and $\widetilde{E}^2A_1$ (panel b) electronic states of B_5.

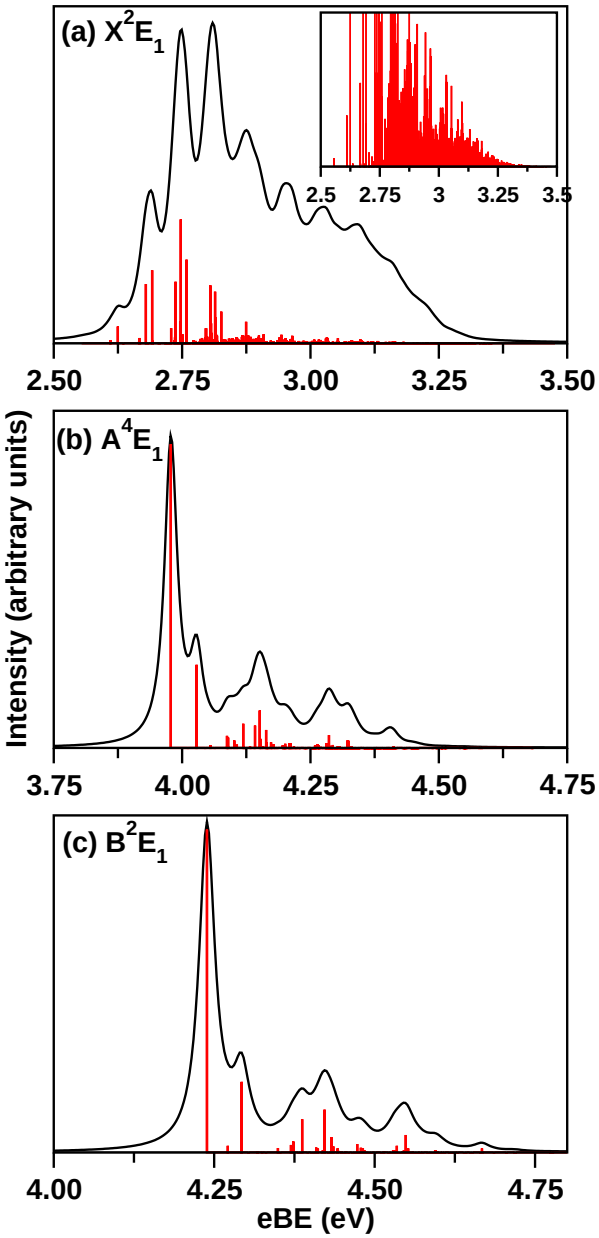

Figure 4.15: Vibronic eigenvalue spectra of $\widetilde{X}^2E_1$, $\widetilde{A}^4E_1$ and $\widetilde{B}^2E_1$ electronic states of the neutral B_7 (isomer I) plotted in panel a, b and c, respectively. The zero of energy correspond to the equilibrium minimum of isomer I of B_7^-. The huge increase of vibronic line density at higher energies resulting from the strong JT effect in the $\widetilde{X}^2E_1$ electronic manifold is shown in the inset of panel a. The numerical details of calculations of the above spectra are given in Table 4.6.

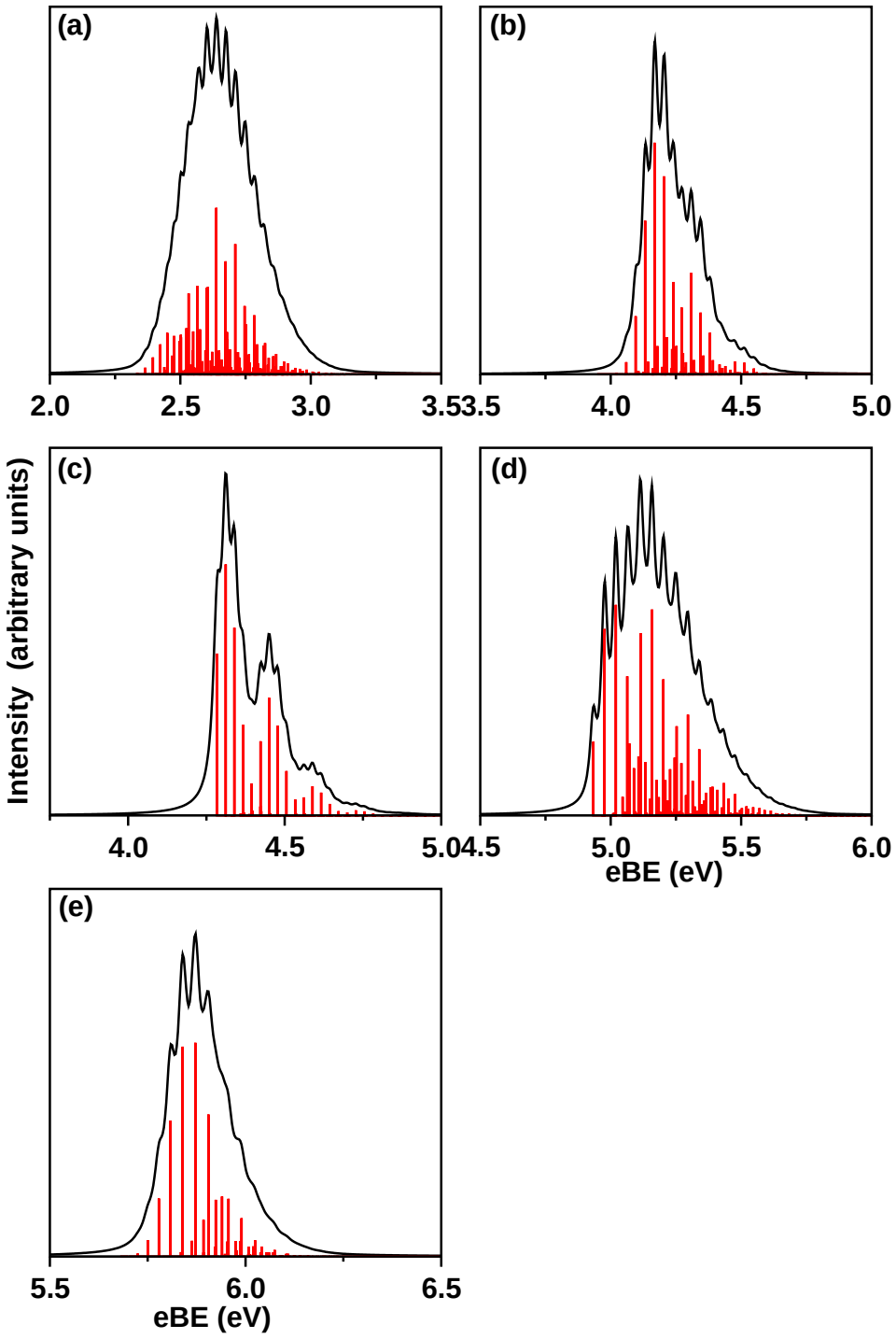

Figure 4.16: Same as in Fig. 4.15, of uncoupled $\widetilde{X}^2B_2$, $\widetilde{A}^2B_1$, $\widetilde{B}^2B_2$, $\widetilde{C}^2A_1$ and $\widetilde{D}^2B_1$ electronic states of B_7 (isomer II). The numerical details of calculations of the above spectra are given in Table 4.7.

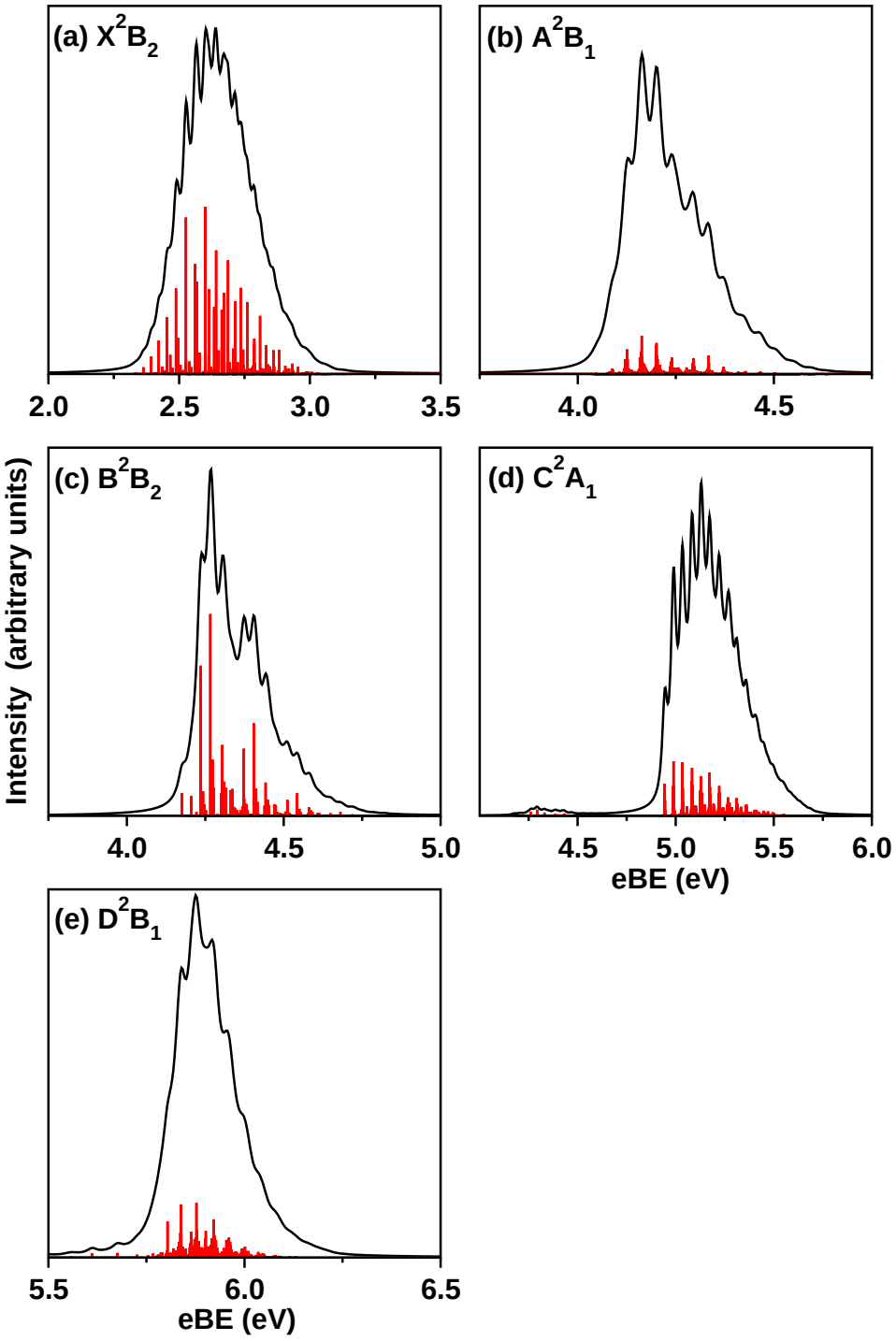

Figure 4.17: Same as in Fig. 4.15, of coupled $\widetilde{X}^2B_2$, $\widetilde{A}^2B_1$, $\widetilde{B}^2B_2$, $\widetilde{C}^2A_1$ and $\widetilde{D}^2B_1$ electronic states of B_7 (isomer II). The numerical details of calculations of the above spectra are given in Table 4.7.

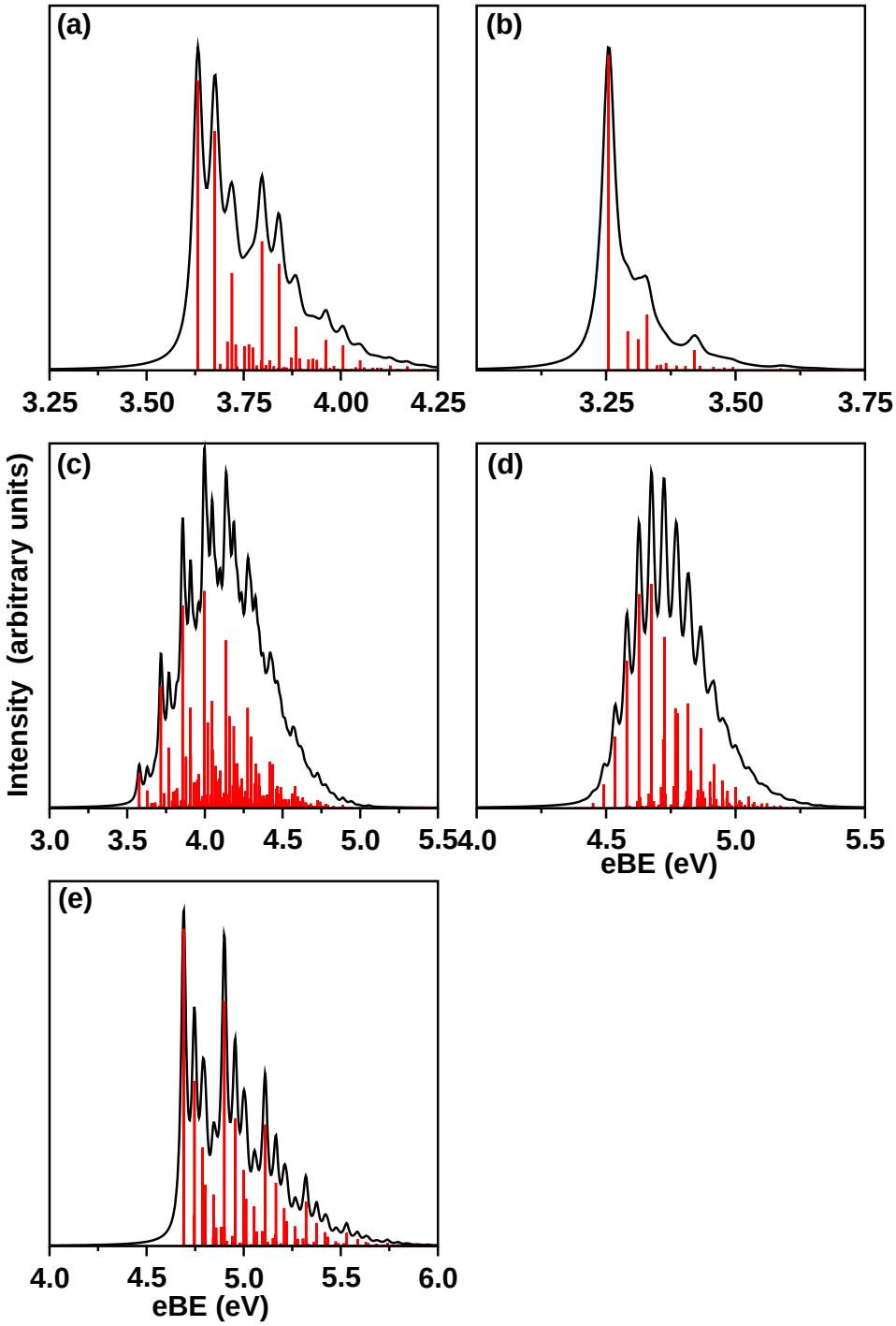

Figure 4.18: Same as in Fig. 4.15, of uncoupled $^2A_2$, $^2B_2$, $\widetilde{B'}^2B_1$, $\widetilde{C'}^2A_1$ and $\widetilde{D'}^2A_1$ electronic states of B_7 (isomer III). The numerical details of calculations of the above spectra are given in Table 4.8.

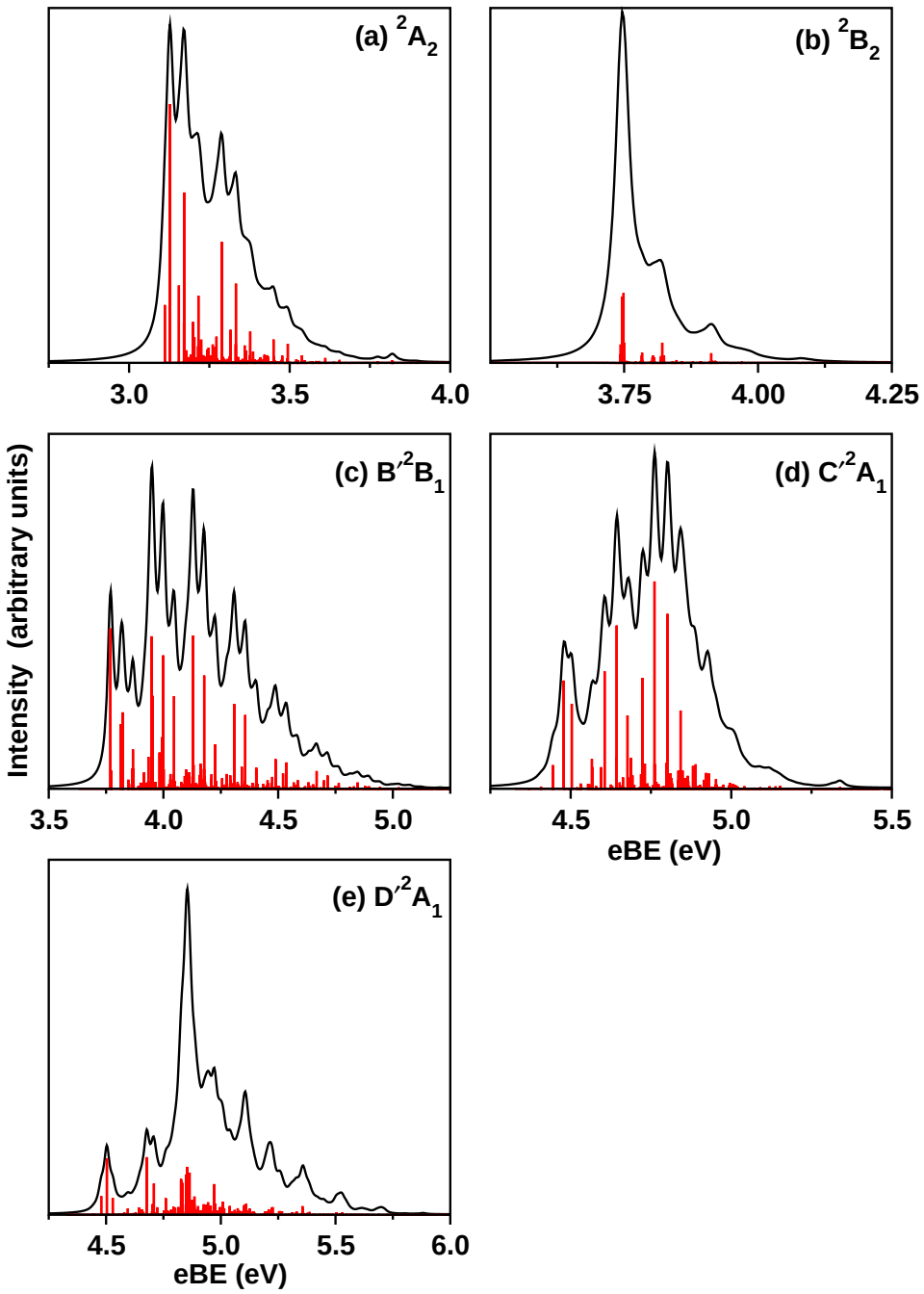

Figure 4.19: Same as in Fig. 4.15, of $^2A_2$, $^2B_2$, $\widetilde{B'}^2B_1$, $\widetilde{C'}^2A_1$ and $\widetilde{D'}^2A_1$ electronic states of B_7 (isomer III). The numerical details of calculations of the above spectra are given in Table 4.8.

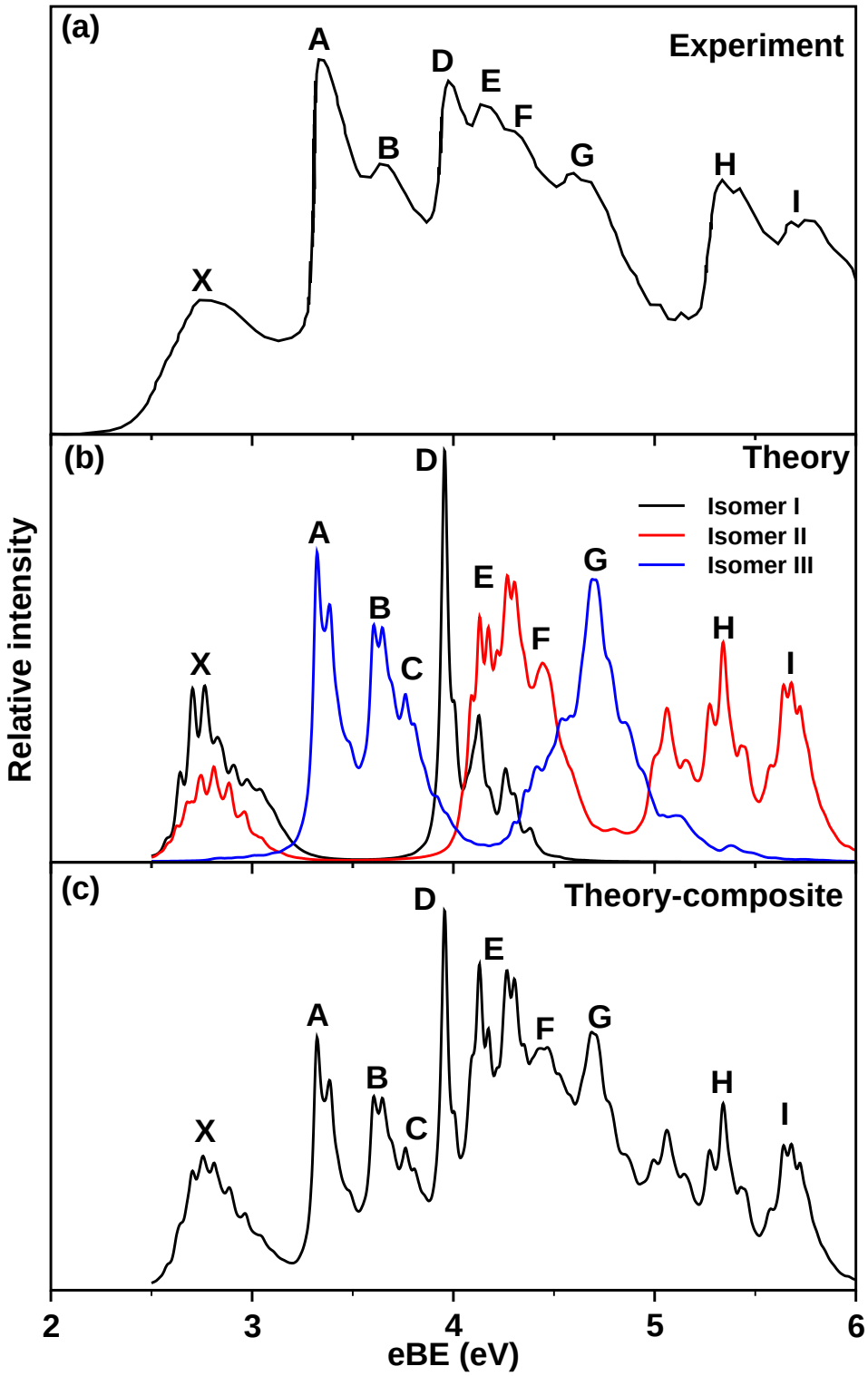

Figure 4.20: Photodetachment spectrum of B_7^-. Relative intensity (in arbitrary units) is plotted as a function of electron binding energy. The 193 nm experimental recording is reproduced from Ref. [4] and plotted in panel a. Theoretical band structure originating from isomer I, II and III of B_7^- is plotted separately in panel b and shown by black, red and blue color lines, respectively (see text for details). The composite theoretical band structure of all three isomers is shown in panel c.

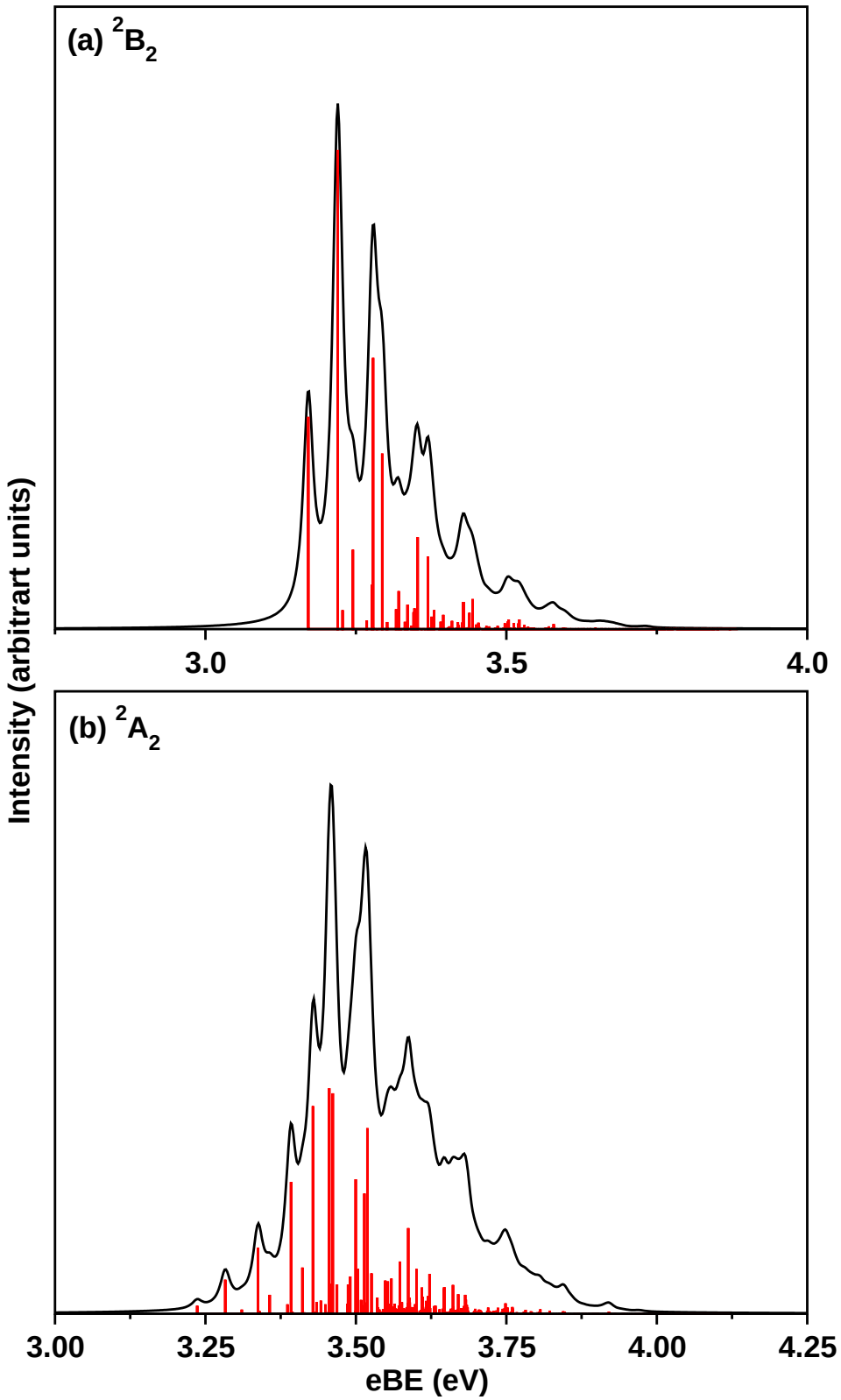

Figure 4.21: Same as in Fig. 4.15, for the $^2B_2$ and $^2A_2$ electronic states of B_7 (isomer III) calculated with the aid of Hamiltonian parameters for the coupled $^2B_2$-$^2A_2$ states extracted from the OVGF energy data.

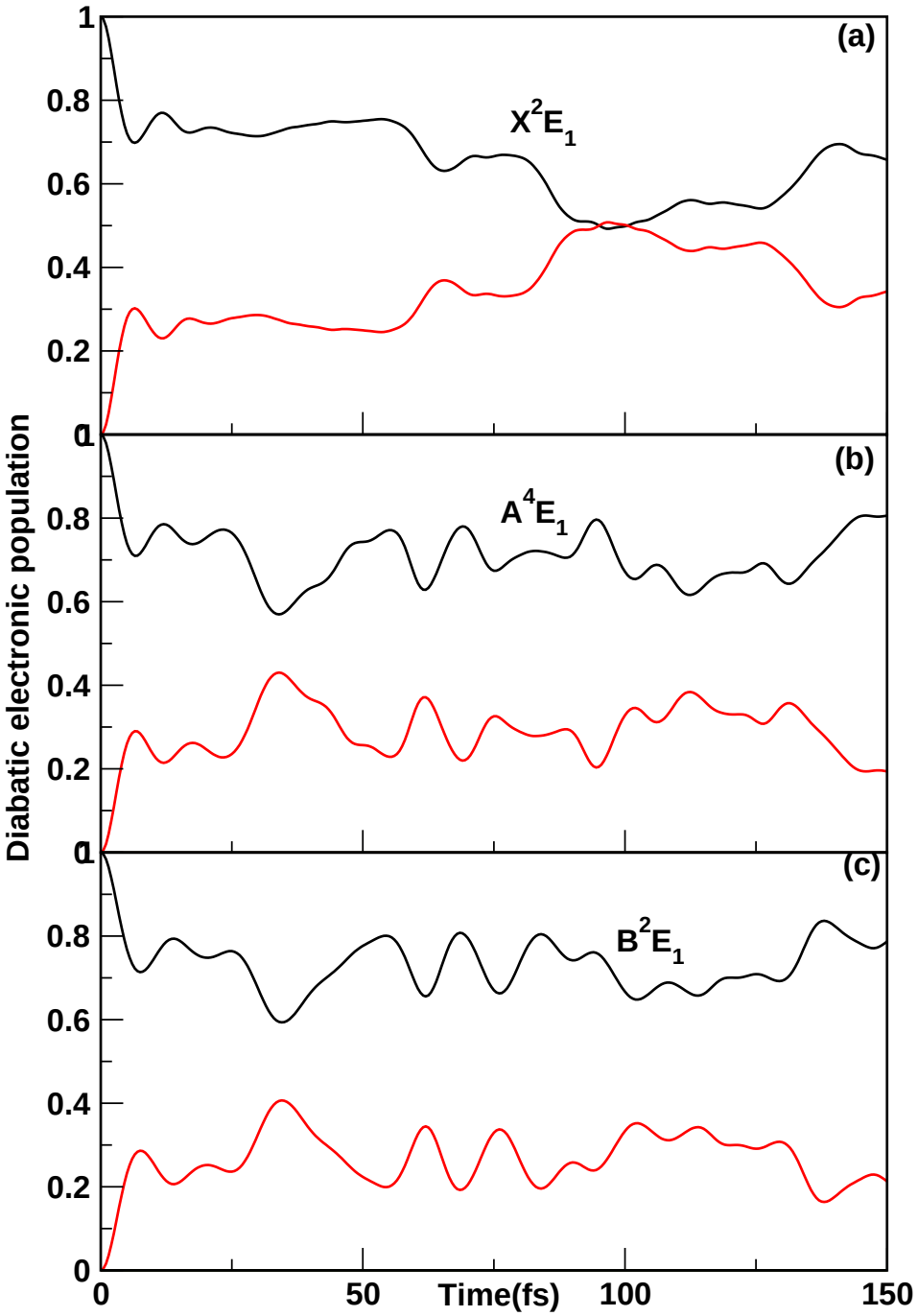

Figure 4.22: Time-dependence of diabatic electronic populations for an initial location of the WP on the $\widetilde{X}^2E_1$ (panel a), $\widetilde{A}^4E_1$ (panel b) and $\widetilde{B}^2E_1$ (panel c) electronic states of B_7 neutral isomer I. The black and red lines in each panel represents the x and y components of the each degenerate state, respectively.

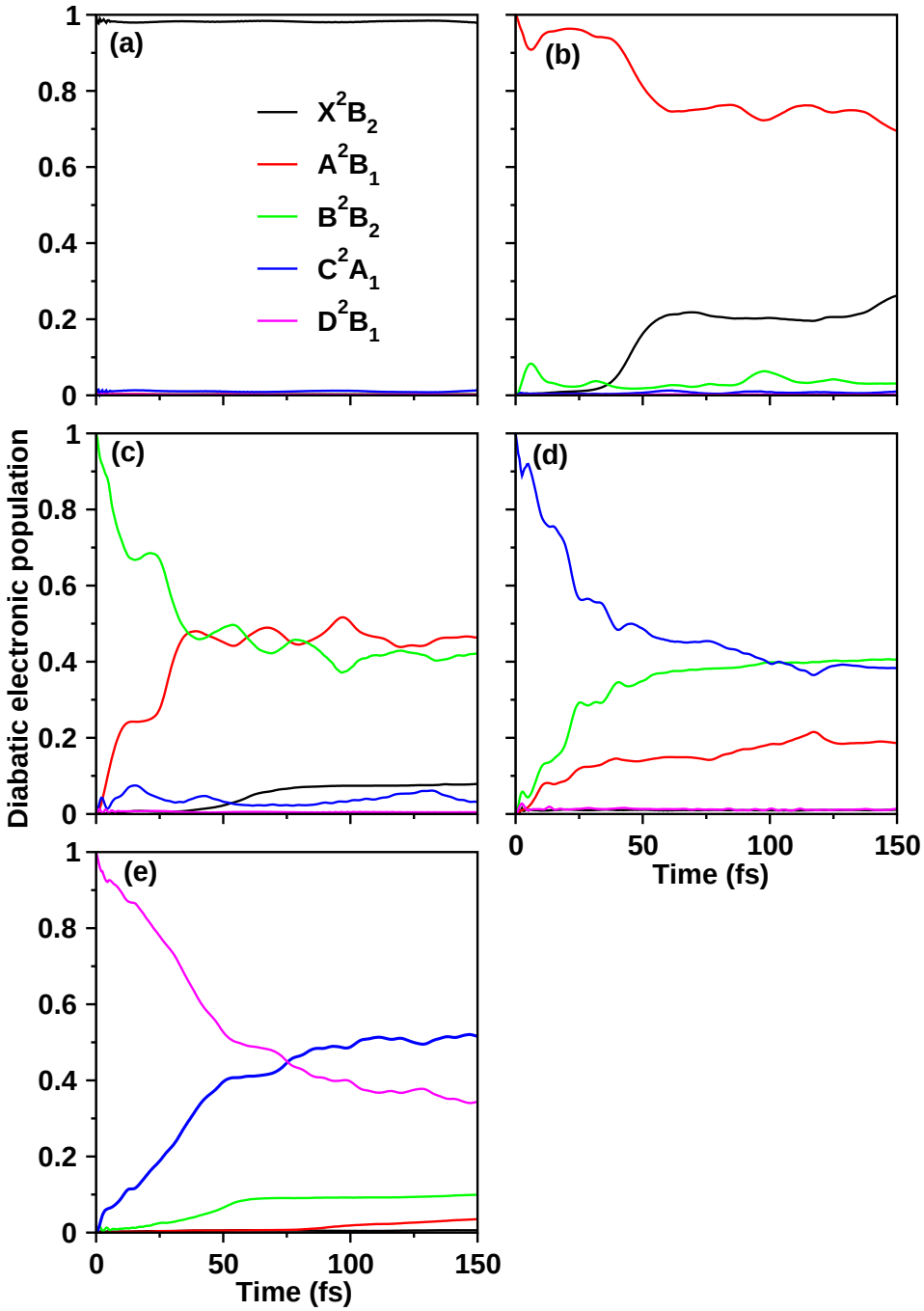

Figure 4.23: Time-dependence of diabatic electronic populations for an initial location of the WP on the $\widetilde{X}^2B_2$ (panel a), $\widetilde{A}^2B_1$ (panel b), $\widetilde{B}^2B_2$ (panel c), $\widetilde{C}^2A_1$ (panel d) and $\widetilde{D}^2B_1$ (panel e) electronic states of neutral isomer II.

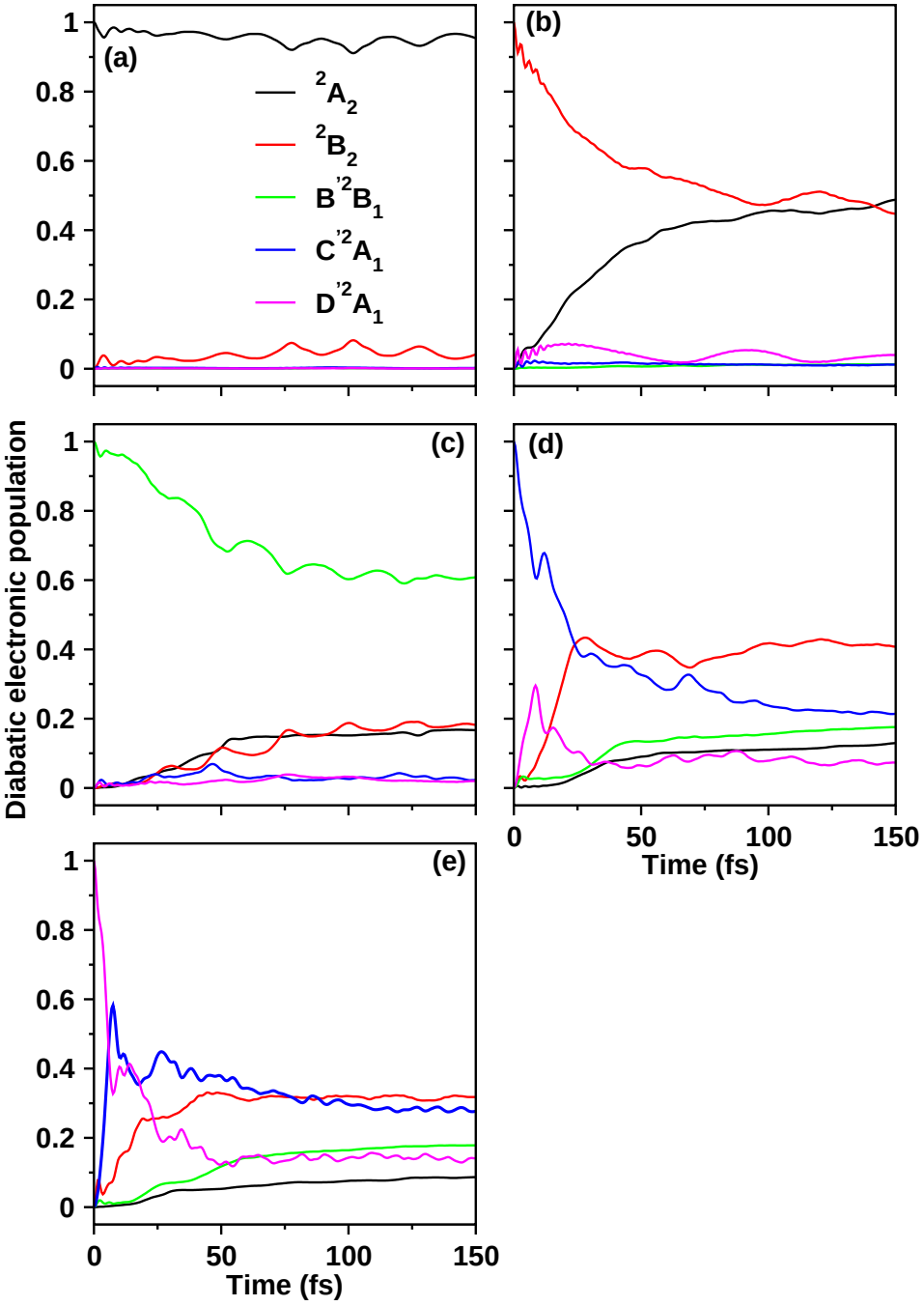

Figure 4.24: Time-dependence of diabatic electronic populations for an initial location of the WP on the $^2A_2$ (panel a), $^2B_2$ (panel b). $\widetilde{B'}^2B_1$ (panel c), $\widetilde{C'}^2A_1$ (panel d) and $\widetilde{D'}^2A_1$ (panel e) electronic states of B_7 neutral isomer III.

References

[1] T. S. Venkatesan, K. Deepika, and S. Mahapatra, J. Comput. Chem. **27**, 1093 (2006).

[2] H. J. Zhai, L. S. Wang, A. N. Alexandrova, A. I. Boldyrev, and V. G. Zakrzewski, J. Phys. Chem. A **107**, 9319 (2003).

[3] H. J. Zhai, L. S. Wang, A. N. Alexandrova, and A. I. Boldyrev, J. Chem. Phys. **117**, 7917 (2002).

[4] H. J Zhai, L-S Wang, A. N. Alexandrova and A. I. Boldyrev, J. Phys. Chem. A **108**, 3509 (2004).

[5] M. T. Nguyen, M. H. Matus, V. T. Ngan, D. J. Grant, and D. A. Dixon, J. Phys. Chem. A **113**, 4895, (2009)

[6] T. B. Tai, D. J. Grant, M. T. Nguyen, and D. A. Dixon, J. Phys. Chem. A **114**,994, (2010)

[7] Conical Intersections: Electronic Structure, Dynamics and Spectroscopy, edited by W. Domcke, D. R. Yarkony, and H. Köppel (World Scientific, Singapore, 2004).

[8] H. Köppel, W. Domcke, and L. S. Cederbaum, Adv. Chem. Phys. **57**, 59 (1984).

[9] M. Born and R. Oppenheimer, Ann. Phys. (Leipzig) **84**, 457 (1927).

[10] M. Born and K. Huang, The Dynamical Theory of Crystal Lattices, (Oxford University Press, Oxford, U.K., 1954).

[11] R. Englman, The Jahn-Teller Effect, (Wiley, New York, 1972).

[12] M. Baer, Beyond Born-Oppenheimer:electronic non-adiabatic coupling terms and conical intersections, (John Wiley and Sons, 2006).

[13] S. Mahapatra, Acc. Chem. Res. **42**, 1004 (2009).

[14] G. A. Worth, M. H. Beck, A. Jäckle, and H.-D. Meyer, The MCTDH Package, Version 8.2, (2000), University of Heidelberg, Heidelberg, Germany. H.-D. Meyer, Version 8.3 (2002), Version 8.4 (2007). See http://mctdh.uni-hd.de.

[15] H.-D. Meyer, U. Manthe, and L. S. Cederbaum, Chem. Phys. Lett. **165**, 73 (1990).

[16] U. Manthe, H.-D. Meyer, and L. S. Cederbaum, J. Chem. Phys. **97**, 3199 (1992).

[17] M. H. Beck, A. Jäckle, G. A. Worth, and H.-D. Meyer, Phys. Rep. **324**, 1 (2000).

[18] J. Cullum and R. Willoughby, Lanczos Algorithms for Large Symmetric Eigenvalue Problems (Birkhäuser, Boston, 1985, Vols. I and II).